A Finite Difference Approach to Modeling High Velocity/Variable Loads using the Timoshenko Beam Model

Alan Joseph Staley

Thesis submitted to the faculty of the Virginia Polytechnic Institute and State University in partial fulfillment of the requirements for the degree of

Master of Science
In
Mechanical Engineering

A.L. Wicks - Chair
Robert West - Member
Christian James - Member

3/18/2011
Blacksburg, VA

Keywords: Timoshenko Beam, Finite Difference, High Velocity Beam Loading, Variable Beam Loading

A Finite Difference Approach to Modeling High Velocity/Variable Loads using the
Timoshenko Beam Model

Alan Joseph Staley

Abstract

Electromagnetic launchers (railguns) are set to replace traditional large caliber ship
mounted cannons in the near future. The success of the railgun depends heavily upon a
comprehensive understanding of beam behavior during periods of heavy dynamic loading. It is
hypothesized that the combination of velocity transition effects, electromagnetic loading, and
other non-linear or design specific effects contribute to areas of high stresses/strains over the
length of the rail/beam during launch.

This paper outlines the use of the Timoshenko beam model, a model which builds upon
the traditional Bernoulli-Euler beam theory with the addition of shear deformation and rotary
inertia effects, a necessity for high wave velocities. Real-world experimental setups are
simplified and approximated by a series of linear springs and dampers for model prediction and
validation

The Timoshenko beam model is solved using finite difference (FD) methods for the
approximation of spatial derivatives and MATLAB ordinary differential equation (ODE) solvers.
The model shows good convergence and precision over a large range of system parameters
including load velocities, foundation stiffness values, and beam dimensions. Comparison to
experimental strain data has validated model accuracy to an acceptable level. Accuracy is
further enhanced with the inclusion of damping and non-linear or piecewise effects used to
mimic experimental observations. The MATLAB software package presents a valid preliminary
analysis tool for railgun beam and foundation design while offering advantages in ease of use,
computation time, and system requirements when compared to traditional FEA tools.

Table of Contents

List of Figures

List of Tables

Chapter 1: Introduction

The analysis and subsequent understanding of beam response under high velocity, accelerating, and variable loading is paramount in designing future electromagnetic launch systems. Considerable research has been documented on both constant velocity and accelerating loads such as those documented in Fyrba's work with the Timoshenko beam model[2], though the methods by which these are solved do not lend themselves well to the non-linear components that can arise in some systems. These include non-linear foundation response, plastic beam deformation, and non-linear beam shape effects. Current finite element (FE) models produce adequate results though they currently require significant time and resource investments. For preliminary design and analysis the extensive complexity of FE modeling is not efficient. This paper proposes a finite difference (FD) approach to solving the Timoshenko beam model using a combination of MATLAB ode solvers and novel code. The FD method and Timoshenko model offer a simplified yet robust analysis tool which balances accuracy and high level modeling with computation requirements. The various capabilities of this approach are discussed throughout this thesis and focus on the enhancing the understanding of the various system components and their impact on beam behavior during launch. Software robustness comes from the simplicity of incorporating additional effects which account for non-linearities and other factors seen during launch. Along with this expandability the program can cover a wide range of beam setups, from small experimental cases to large full-scale designs, thus giving future designers the tools needed to quickly compare novel designs.

A beam's behavior under load, constant or varying in magnitude, is known to change for a variety of traversing velocities [1] [2]. It is believed that these effects attribute to various locations of high stress levels within a beam or structure when experiencing this type of loading. The conducting beams used by the railgun, sketched in Figure 1, are predicted to show significant displacement when the weapon is in use [11]. While some of this is due to the transverse electromagnetic loading, the levels of beam deflection, distortion, and wear seen after launches indicate additional model components are required for an accurate analysis. Adding such effects can enhance the Timoshenko beam model for this unique application involving both high speed and large magnitude time dependent loads. Analyzing the effect of the various system components on the behavior of the beam during launch will aide in future development of weapon bore life and efficiency. The software package and model presented in this paper are meant to compliment the FEA packages currently in use by providing a set of base level analysis tools for design evaluation. Solving the model using the FD approach allows for the relatively simple inclusion of both linear and non-linear effects that are being discovered during experimental projectile launch and efficient analysis of individual system components. Testing various novel design components such as non-uniform beam or foundation shape prior to FE simulations or experimental models saves both time and financial resources.

This thesis is divided into six additional sections: *Railgun Background, Beam Models and Implementation, Applied Timoshenko Beam Theory, Railgun Finite Difference Validation, Dynamic Load Factor and MATLAB User Interface,* and *Future Work and Conclusion.* The *Railgun Background* section will deliver a brief overview of the railgun system, issues facing the development and success of the program, and current analytical methods. *Beam Models and Implementation* delves into the various components of the Timoshenko model and the loading methods used to approximate real-world loading. Additionally, the spatial derivative approximations by way of the finite difference method and boundary conditions used are discussed. The application of the Timoshenko model to a known experimental setup is discussed in the *Applied Timoshenko Model* section; the results of this implementation are presented in *Railgun Finite Difference Validation*. The addition of the Dynamic Load Factor analysis tool and the graphical user interface description are included in the *Dynamic Load Factor and MATLAB User Interface*. Finally, a short discussion outlying the *Future Works/Conclusion* for this project and potential areas of interest in railgun beam analysis.

2.1   Railgun Basics

An electromagnetic launcher, otherwise known as a railgun, relies solely on electromagnetic effects to propel a projectile to hypersonic speeds, i.e. velocities approaching Mach 8, without the help of conventional explosive propellants. These systems require high levels of electrical current surging through two parallel beams and a sliding armature; which acts as a short between the beams. Coupled with the magnetic fields produced by the current in the rails, a Lorentz force is generated which launches the projectile from the weapon [4]. Figure 1, gives a simplified view of the basic components of a railgun and the forces and fields involved in launching the projectile. The vertical connection shown in Figure 1 represents the armature/projectile package which carries the current load during launch so as to ensure the integrity of the projectile after it leaves the weapon. As stated before, the interaction of the magnetic fields around the two beams with the current flowing through the armature creates the propelling force, a force normally provided by chemical explosives in conventional weaponry.
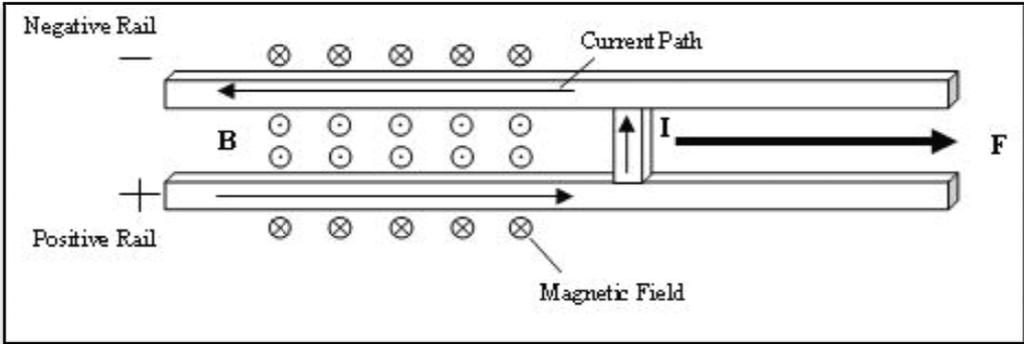
Figure 1: Simplified Railgun Schematic

The magnetic fields generated are shown as the arrow heads wrap above and below the rails. The solid arrows shown within the rails represent the current path during launch as it flows through the high potential rail, through the armature, and back through the second rail. The weapon is designed such that the magnetic fields around the beams align behind the armature in the correct manner to propel the armature forward. In Figure 1 the fields between the rails are aligned out of the page and from basic electrical theory the force, F, exerted on the armature/projectile is a cross product, of the current, I, and the magnetic field, B, shown in Equation (1).

$$\vec{F} = \vec{I} \times \vec{B} \qquad (1)$$

The forces generated are powerful enough to launch a 5.12kg projectile at approximately Mach 7.2(2500 m/s) within a few milliseconds. Chapter 3.4 will show that this velocity range is the same order of magnitude as the various wave velocities associated with a railgun setup thus creating the additional design problems currently seen in experimental setups.

The opposing currents in the two rails cause a repulsive force between them, given by Equation (2). This force is the primary cause of the displacements and subsequent stresses the beam experiences during a projectile launch. A containment structure is designed around the two rails to prevent both longitudinal and lateral destruction of the railgun due to the repulsive forces and/or the reaction forces from the armature launch. Thus designing the containment for a specific weapon setup can rely heavily on the anticipated loading between the conducting rails.

$$P = \frac{I^2 \mu_0}{2\pi d} \qquad (2)$$

Here the force per unit length, P, is defined by the current I in amps, permeability of free space μ_0, and the distance, d, between the beams in meters. For all calculations μ_0 is given to be $4\pi*10^{-7}$ N/A^2. The containment is required to resist the repulsive force for all locations on the beam where current is flowing, thus all locations behind the armature. The load is not uniform as it changes with the square of the current supplied by the capacitors. A variety of current discharge profiles could be used which cause the beam and containment to experience very fast loading and unloading situations. While the basic physics of a railgun are quite simple, the intense joule heating, high projectile velocity and current levels coupled with the short duration of the launch make the successful implementation of such a weapon a complicated task.

2.2   Research Justification

The railgun has seen great strides along with the development of supporting technologies such as rail and containment materials, improved capacitors and containment designs. What were once small proofs of concept designs with around 8 MJ [5] or lower[6], are now full scale launchers with energies reaching in excess of 32MJ. Armatures are achieving new velocities, and the stresses imparted on the beams are becoming ever greater. Beams loaded to this extreme are predicted during simulations to experience plastic deformation over significant portions of their length. Plastic deformation signifies that stresses within the beam have exceeded the elastic limit. Additional loading, and therefore stressing, past this point reduces the bore life and effectiveness of the weapon as a whole, so much so that the weapon may become inoperable. Correct prediction and resolution of these issues prior to construction becomes a necessity.

Additional problems arise during a projectile launch, including rail gouging [2], electrical arcing [7], melting of the armature and beam surface (caused predominately by joule heating, arcing, and friction), metal deposition and rail pitting. Many of these occurrences compound upon one another during a launch thus reducing bore life and railgun efficiency. A brief overview of several additional efficiency components are discussed by Bauer [5]. The combination of these effects could even serve to dislodge the rails or rip the weapon apart and though many hypotheses have been made regarding the various causes, unless significant research and modeling are performed, it is only guess work.

In recent years, with the advent of full scale experimental setups, the modeling, understanding, and reduction of each of these effects has become ever more important and complex. Computational models and the machines used to solve them have developed along with the advancement of the railgun. Current analysis techniques predominately use finite element software such as LS-DYNA or ANSYS to predict the behavior of beams and the surrounding containment under loading, both mechanical and electromagnetic. The systems that are modeled, i.e. the rails, armature, and surrounding containment, are incredibly complex and are becoming increasingly so with each subsequent iteration. Advanced software packages can begin to handle such things as surface Rayleigh waves, a potential cause of surface pitting, armature skipping (uneven armature pressure application) and arcing due to beam wave interactions, and even the effects of surface coating due to the melting of the armature and rails [8]. Such systems are helping engineers grow closer to understanding the underlying causes of failure, or rather, inefficiency during use.

As with any design, a comprehensive analysis of the entire system is not required, nor is it efficient to do so, in the initial stages of the development cycle. Several models have been created for lower level wave propagation and beam behavior which neglect several of the effects discussed before. These are usually only single dimensional in space and show basic beam deflection during launch. Two papers [1] [8] illustrating the effect of armature shape indicate that the problem of discontinuous contact can be reduced by the use of "C-shaped" armature. When the armature breaks contact with the rails, the voltage within the system increases as arcing occurs. This arcing causes additional wear and damage to the rails in addition to causing additional heat generation and a variety of other detrimental effects. To this end the modification and analysis of new rail/foundation designs in coordination with novel armature designs can alleviate some of these problems. Johnson and Moon use a combination of ANSYS finite element software for analysis of the armature with the analytical Timoshenko beam model on an elastic foundation for the two rails, Figure 2.   The G-10 insulation material used in modern railgun design can be roughly approximated as a series of linear springs coupled to the rail. Modeling the containment also includes damping effects which are briefly discussed in Chapter 3: Timoshenko Beam Theory.
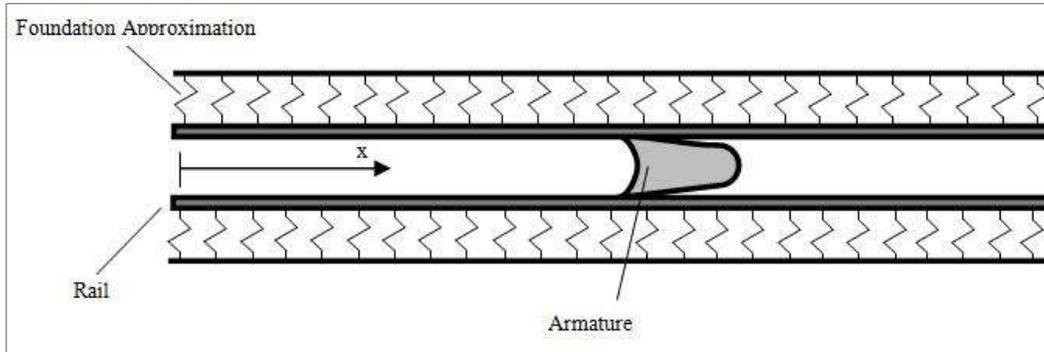
Figure 2: Simplified railgun/armature on elastic foundation

This model incorporates shear and rotational inertia effects in addition to traditional one dimensional beam mechanics to provide advanced wave propagation dynamics. The merging of the Timoshenko beam and FE analysis of the armature is able to predict pressure spikes seen during launch as the speeds increase [1].

The simplified Timoshenko beam model is ideal for early system development as it offers a less complex and computationally intensive analysis of the beam behavior prior to the use of full finite element packages. Further development of these models would need to include other non-linear effects, such as discontinuous system parameters, non-linear springs, or perhaps additional components meant to mimic effects seen during experimentation. The Timoshenko beam model is quite robust in that it allows for the addition of such components with relative ease. Shifting the focus of system analysis back to the deflection behavior and stresses within the beam, the Timoshenko model provides a valid preliminary tool for the studying of novel designs. It is the purpose of this thesis to define an accurate, fast, and straight forward solution method and software construct for the analysis of the Timoshenko model.

2.3   Scope of Software Analysis

Though rail behavior during launch is a complex combination of many factors, as mentioned in greater detail in sections 2.1 and 2.2, key features of this behavior have yet to be fully realized and understood, particularly armature velocity and load application. The proposed FD software package generates rail responses based solely on these two effects and, while intentionally simplistic, the results define a baseline for the complex motions seen in the experimental setup.

As previously stated, beam deflection and applied forces are predicted only in the direction normal to the beam's length. Using this model the researcher is acknowledging that while longitudinal motion and forces exist, they play a secondary role to transverse loads when predicting beam response. An analysis of these effects, the longitudinal motion and loads, is best developed following a thorough understanding of transverse load behavior. Coupling various loading methods with armature velocity generates complex beam behavior, as discussed further in Chapter 4. Despite the lack of high level effects and multi-dimensional motion, significant

knowledge can be gained through the fast and accurate modeling of the beam using various system and launch profile parameters.

Armature velocity effects depend heavily on system parameters; these include both rail material properties and foundation stiffness. The modification of these values and their respective impact on rail response will assist with current efforts towards a comprehensive understanding of the railgun system. Further discussions of these effects are seen in section 3.4, Chapter 4, and Chapter 6. Data generated by the simulator can be saved and analyzed as the user sees fit, though it is ultimately the qualitative understanding of beam behavior and ability to compare designs that justifies the software's use.

Chapter 3: Beam Models and Implementation

3.1   Beam Models

Defining a beam model that is fast, accurate, and robust enough to incorporate and predict the various linear and non-linear beam behaviors that can be encountered within the railgun began by first defining a beam. As two and three dimensional models were beyond the complexity required for the software package, the one dimensional Bernoulli-Euler beam became the starting point for design analysis.

3.1.1   Bernoulli-Euler

Traditional beam theory is derived using force and moment balances on a beam, or more specifically, a beam element, as shown in Figure 3. In the figure a simplified free-body diagram gives an overview of the various forces and moments acting upon an element at any one time step. As the figure depicts, for this beam model the cross-section is assumed to be non-deformed and normal to the beam centerline for all displacements. Bernoulli-Euler also assumes that the transverse displacements are extremely small and the beam length is comparatively much larger than the dimensions of the cross-section (20:1 or greater), often referred to as a slender beam. No nodal rotation effects are taken into account for this preliminary model.
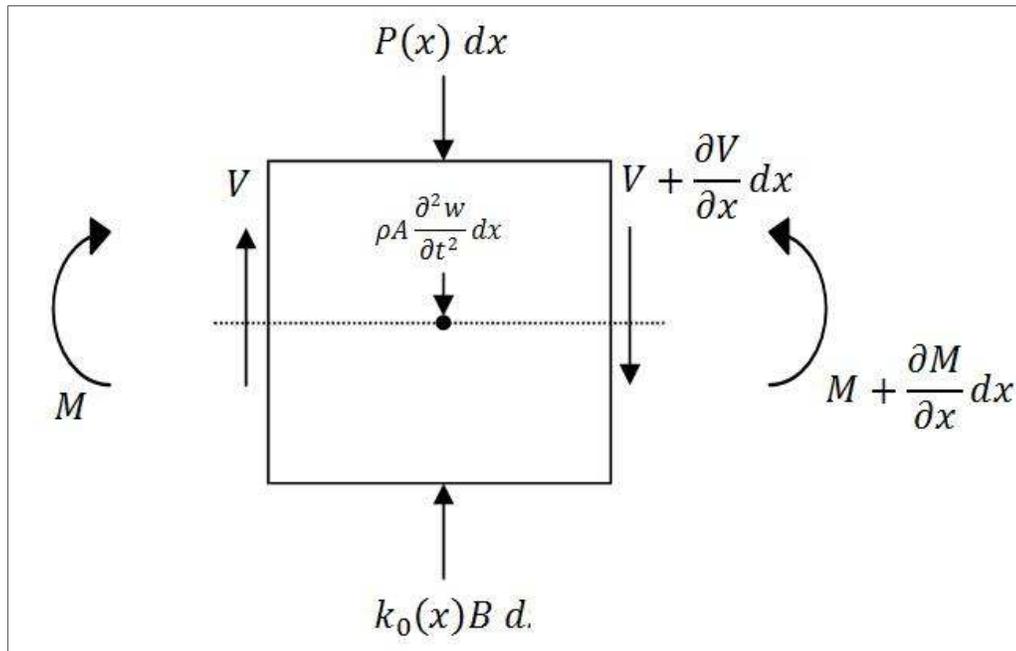
Figure 3: Bernoulli Euler Beam Element with acting forces and moments

Here $P(x)dx$ represents the external loading applied to the element, $k_0(x)w\,dx$ is the proportional restorative force provided by the elastic foundation, and $\rho A\,d^2w/dt^2$ the kinetic motion term. The moment and the change in moment across the node are represented by $M + \partial M/\partial x$ and in a similar way the shear force and change in shear over dx are given by $V + \partial V/\partial x$. As discussed in Weaver, Jr. and Timoshenko [10], the translational force balance is given by,

$$V - V - \frac{\partial V}{\partial x} - \rho A \frac{\partial^2 w}{\partial t^2} + k(x)Bw\,dx = P(x)dx \tag{3}$$

the moment balance is

$$-Vdx - M + M + \frac{\partial M}{\partial x}dx \approx 0 \tag{4}$$

Knowing the moment acting on the element can be related to the displacement by

$$M = EI\frac{\partial^2 w}{\partial x^2} \tag{5}$$

and combining Equations (3), (4), and (5) to obtain a version of what is known as the Bernoulli-Euler beam on an elastic base, a definition for the deflection of the beam is derived. Given as Equation (6), the Bernoulli-Euler model predicts beam behavior for a variety of inputs and system conditions.

$$EJ\frac{\partial^4 w(x,t)}{\partial x^4} + \rho A\frac{\partial^2 w(x,t)}{\partial t^2} + k_0(x)Bw(x,t) = P(x,t) \tag{6}$$

The various quantities used to describe the beam behavior are listed in Table 1.

Table 1: System and Timoshenko Parameters

Symbol	Description	Units
$w(x,t)$	Transverse displacement	m
$P(x,t)$	Loading per unit length	N/m
E	Modulus of elasticity	GPa
J	Cross-sectional moment of the rail	m^4
ρ	Beam material density	kg/m^3
A	Cross-sectional area of the beam	m^3
B	Beam width	m
k_0	Foundation stiffness	N/m^3

The Bernoulli-Model provided a simple test case for the finite-difference approach, approximating the behavior of railgun systems. The assumptions made when deriving this model are not valid when analyzing situations in which high wave frequencies are expected. As the wavelengths become shorter the model will not limit the speed of these waves, allowing for infinite wave velocities which are physically impossible and generate erroneous simulation results. Wavelengths for these speeds are approaching that of the beam dimensions and require greater complexity to accurately model.

With the simplified model, the low deformations of a slender beam do not apply for a railgun beam. Unlike conventional beams analyzed by the Bernoulli-Euler model, such as railways, railgun beams are far broader and short, with cross-section to length dimension ratios lower than 1:20. Rotation of each individual node and the effect of shear on the lateral displacement slope have a significant role on the beam behavior. This requirement leads to the need for a slightly more complex model, the Timoshenko Beam.

3.1.2   Timoshenko Beam model

The Bernoulli-Euler beam is actually a special case of the more general Timoshenko Beam which accounts for both rotational inertia and shear deformation, shown in Figure 4.
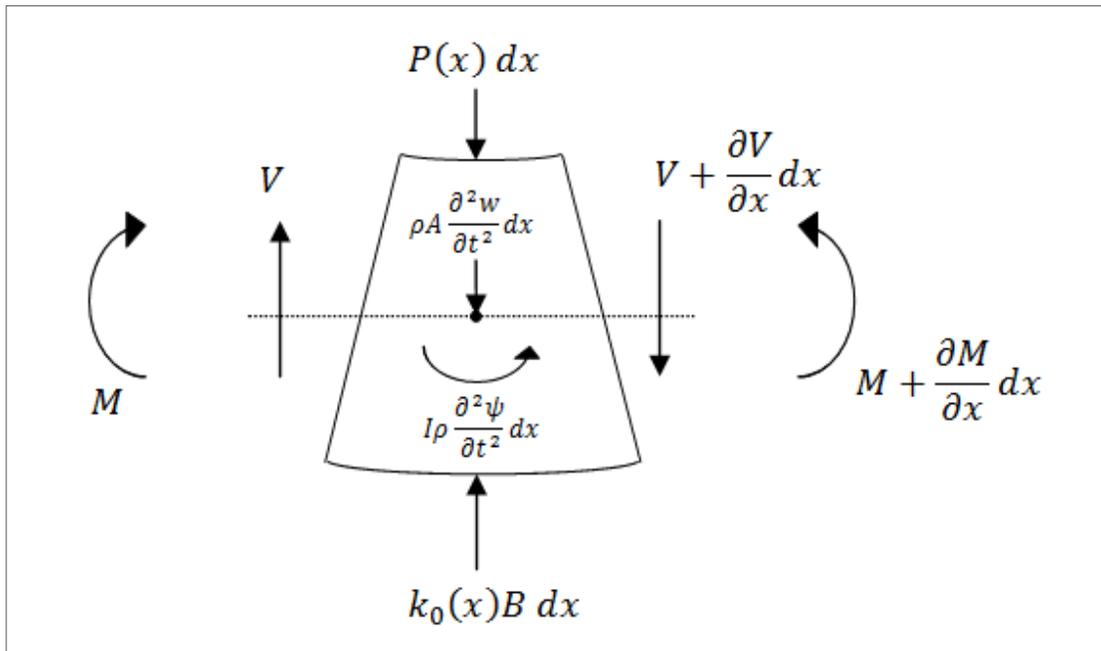
Figure 4: Timoshenko beam element with external forces

Incorporating these two effects changes the translational force and moment equilibrium equations into,

$$\kappa GA \left(\frac{\partial^2 w}{\partial x^2} - \frac{\partial \psi}{\partial x} \right) - \rho A \frac{\partial^2 w}{\partial t^2} + k_0(x)Bw = P(x) \tag{7}$$

$$EI \frac{\partial^2 \psi}{\partial x^2} + \kappa GA \left(\frac{\partial w}{\partial x} - \psi \right) - \rho I \frac{\partial^2 \psi}{\partial t^2} = 0 \tag{8}$$

where ψ is the slope of the deflection curve without the effects of shear, G, is the beam shear modulus and κ, the Timoshenko shear coefficient which accounts for the beam's cross-sectional shape. Equation 7, the translational force balance, remains nearly the same except for the change in vertical component of shear, which is now modified by the shear deflection term. The second term in Equation 8 represents the effects of shear deformation on the beam element, as the shear slope due to the imparted load is the difference in the total rotation of this element compared to an element in which there is no shear deformation. The third term defines the rotational inertia effects. The two second order partial differential equations can be combined into a non-linear 4th order differential Equation (9), this became a more intuitive model for the addition of more terms and implementation into MATLAB. A detailed explanation of this process is given in [10].

$$\underbrace{EI \frac{\partial^4 w(x,t)}{\partial x^4} + \rho A \frac{\partial^2 w(x,t)}{\partial t^2}}_{\text{Bernoulli-Euler}}$$

$$\underbrace{-\rho I \left(1 + \frac{E}{\kappa G} \right) \frac{\partial^4 w(x,t)}{\partial x^2 \partial t^2} + \frac{\rho^2 I}{\kappa G} \frac{\partial^4 w(x,t)}{\partial t^4}}_{\substack{\text{Rotational Effects} \\ \text{(Inertia/Shear)}}} + \underbrace{k_0 Bw(x,t)}_{\substack{\text{Foundation} \\ \text{Restoration} \\ \text{Force}}} = \underbrace{P(x,t)}_{\text{External Loading}} \tag{9}$$

Two time derivative terms, the acceleration of the moment and a fourth order term have been added to the Bernoulli-Euler model. As mentioned in [1] this model resolves the infinite wave speed issues and more accurately predicts high frequency vibrations. In this form it is easy to incorporate additional effects to the model, such as viscous damping (10) or non-linear effects that may enhance its accuracy.

$$C\frac{\partial w(x,t)}{\partial t} \qquad (10)$$

Here C is the damping coefficient, with units of N-s/m, this value is approximated for the given simulations until a more definitive value can be determined through experimentation.

For the Timoshenko model it is interesting to note that the added rotation term is affected much more by deformation due to shear than the rotational inertia of the element. For the case presented in this paper this ratio is approximately 3.2:1.

3.1.3 Boundary Conditions

For a beam supported, or not supported, on two ends a variety of boundary conditions are possible. Fixed, pinned, and free ends are the most commonly used. Fixed ends are without displacement or slope while pinned ends, also referred to as a simply supported, have no translation or moment. The most commonly used boundary condition was the free end. These are without shear or moments and, as the description suggests, are free to move transversely. Table 2 lists these conditions in terms of displacement.

Table 2: Boundary conditions and corresponding derivative representations

Boundary Type	Conditions	
Fixed	$w_{0,L} = 0$	$\dfrac{\partial w_{0,L}}{\partial x} = 0$
Pinned (Simply supported beam)	$w_{0,L} = 0$	$\dfrac{\partial^2 w_{0,L}}{\partial x^2} = 0$
Free	$\dfrac{\partial^2 w_{0,L}}{\partial x^2} = 0$	$\dfrac{\partial^3 w_{0,L}}{\partial x^3} = 0$

The pinned and free boundaries are two most likely conditions used when analyzing rail behavior with the free boundary being the most realistic. Pinned conditions could be used in the experimental stage so as to allow for the slope of the beam to change.

3.2 Force Inputs

Force is applied to the beam via several methods: impulse, electromagnetic projectile launch approximation, and a third constant force accelerating load labeled the dynamic characterization input.

3.2.1 Impulse

Significant aliasing issues are encountered when applying a simple step or Dirac delta function due to the high frequency content present during the instantaneous input change; this prevents accurate simulation of the beam and creates computational errors within the programming environment. To alleviate these issues the impulse is approximated as a decaying sinusoid, commonly referred to the 'sinc' function. The sine wave is limited to 5000 Hz oscillation frequency, it is windowed using a Gaussian window, and shifted in time to half of the simulation time, similar steps have been taken by Iglesias, Wicks and Schwartz [3]. The approximation function is given in Equation (11) and shown in Figure 5 for a 3 millisecond simulation.

$$sinc\ \omega_c(t - t_{shift}) = \frac{\sin \omega_c(t - t_{shift})}{\omega_c(t - t_{shift})} \tag{11}$$
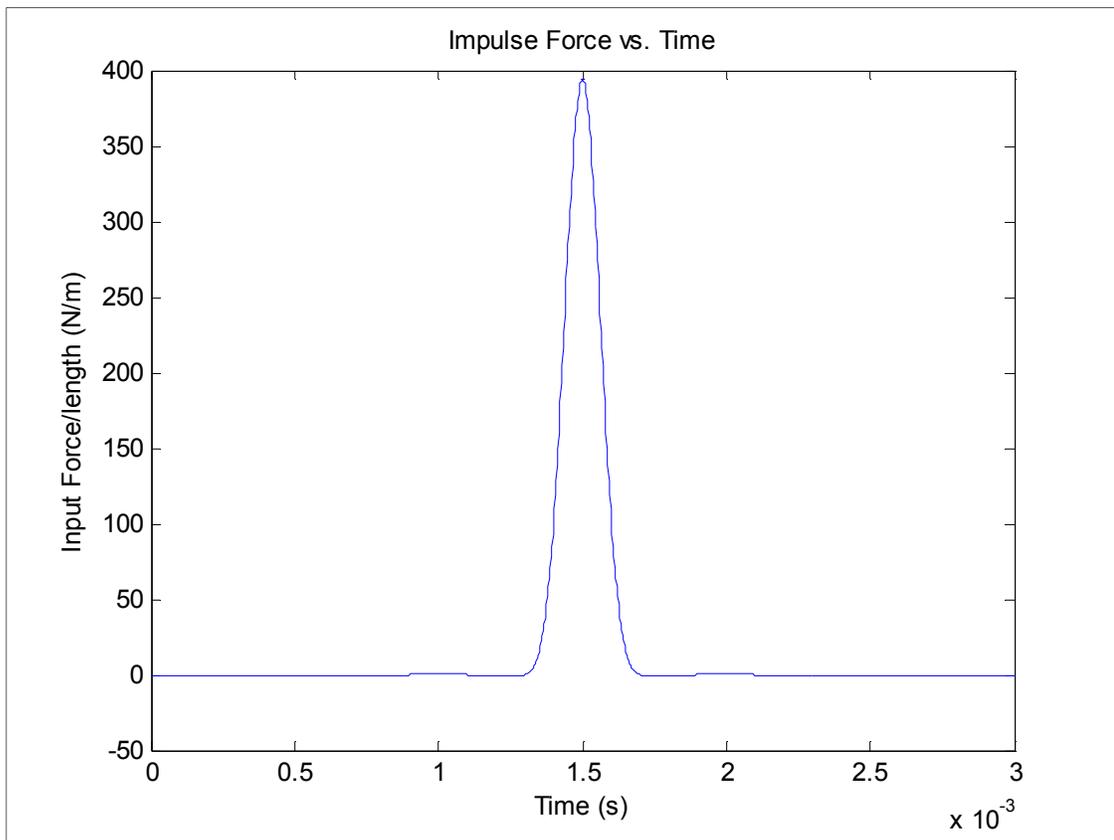
Figure 5: Impulse input approximating sinc function

With ramp up and decay time of about 0.25 milliseconds which are nearly half of the ramp time used during a small scale simulated railgun launch, discussed in section 3.2.2, the

aliasing effects were reduced to an acceptable level. Beam behavior was realistic and the computational errors were alleviated without the need to use large quantities of spatial nodes.

3.2.2   Simulated Launch Profile

The second input is the simulated launch profile. This input requires a user defined time-dependent position/current profile in the form of a Microsoft Excel spread sheet. The software package uses a MATLAB cubic spline fit to approximate the two curves for future use. A sample shot profile is shown in Figure 6 for a 1500m/s projectile exit velocity.
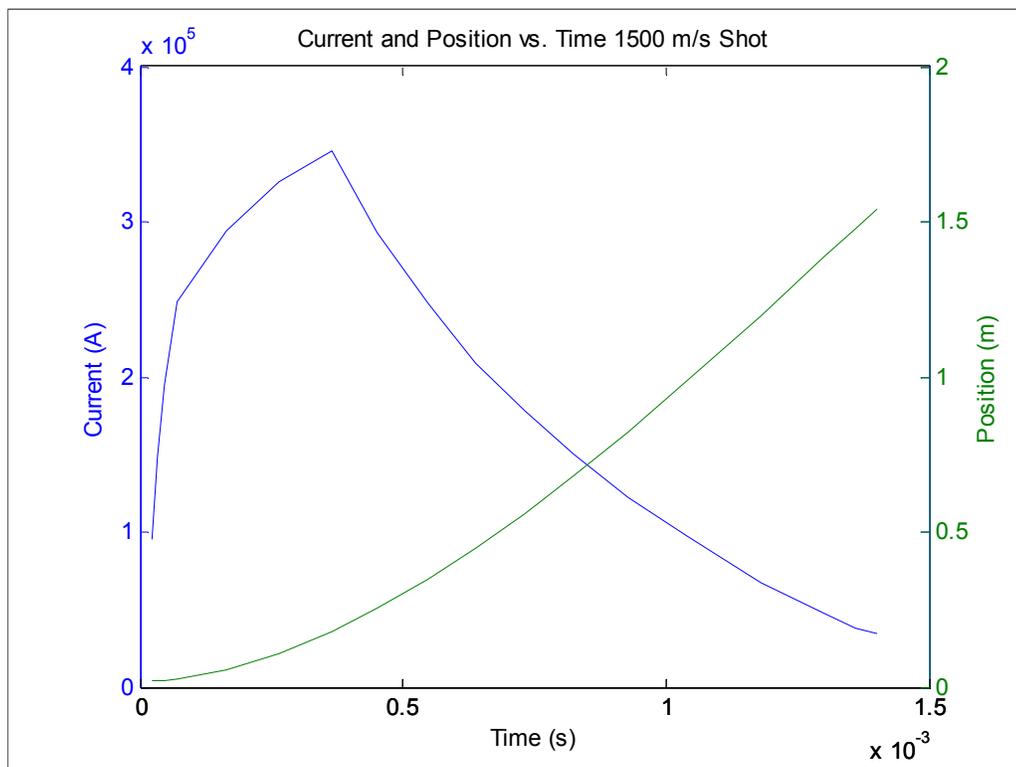
Figure 6: Sample position and current input profile

The spline allows the program to interpolate a position and current value for each of the thousands of time steps when given a relatively low quantity of specified values. In testing, a fit of less than 20 values was able to accurately describe this curve over the duration of the shot, thus reducing the size and complexity of the input files needed. Though this profile is simply shaped, more complex profiles can and have been modeled with high levels of success. Figure 7 depicts the spline fit for the profile shown in Figure 6.
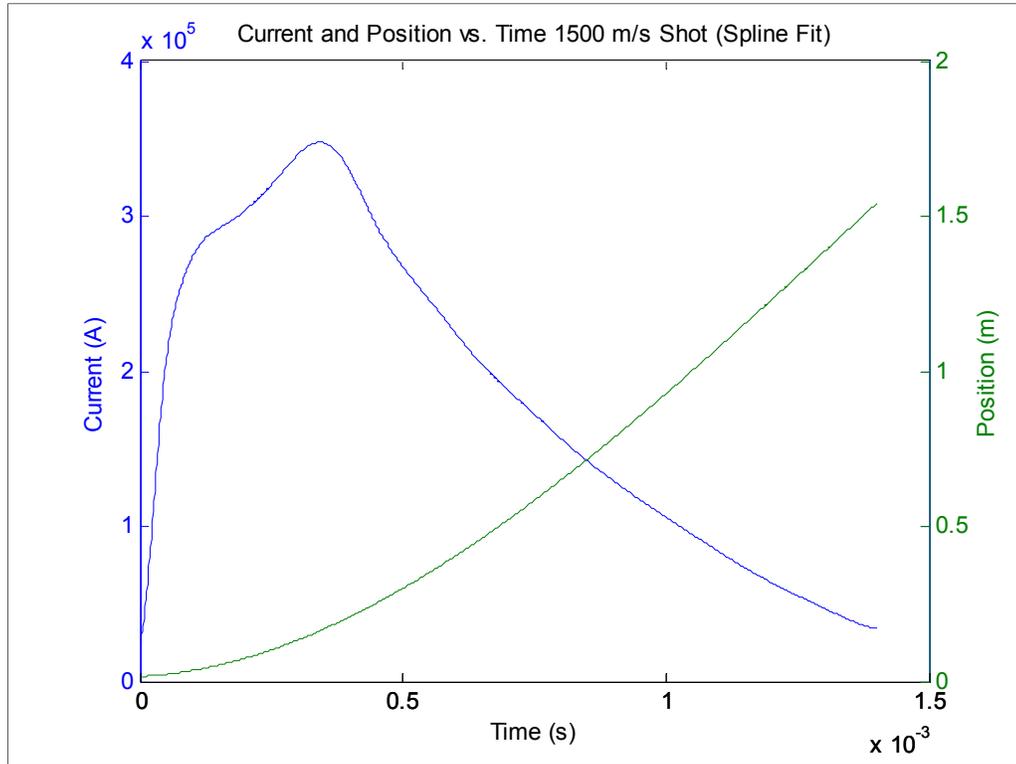
Figure 7: Spline fit of position and current shot profiles

As the projectile traverses the beam, velocity is approximated using backwards difference approximation and is primarily used as a visual aide to the user; all calculations are based purely off the position spline and its change over time. This is crucial when visualizing the changes in beam behavior as the load accelerates through the various velocity regimes.

Nonlinear effects can be added to modify this force for various behaviors such as loss of armature contact due to skipping, which creates uneven loading along the length of the armature. By adding this effect (requiring the force to be proportional to the ratio of critical velocity to instantaneous velocity) the beam behavior could be changed to match the given data to a greater degree. Further research into the area, in conjunction with experimental data, would create a more realistic model for future simulations.

Projectile shape effects are also easily implemented to account for the higher electromagnetic repulsive forces near the rear of the armature. These effects are included within the individual ordinary differential equation (ODE) function definitions modifying the magnitude of the applied force for different locations along the beam as related to time and/or velocity. For the purpose of this paper, projectile shape effects were not included, though have been tested and perform as expected, increasing the stresses at the front of the load and changing the beam deflection behavior over the length of the armature.

3.2.3 Dynamic Characterization Input

The constant force, constant acceleration dynamic characterization input is applied in a similar manner to the projectile launch though the speed and location along the rail are determined in a simpler fashion. User inputs specify an initial and final velocity with a constant force value or amperage; the software calculates the simulation time needed for the projectile to accelerate to the end of the beam while attaining the desired velocity. A linear period of ramping similar in duration to the shot simulation input is included to remove the aliasing problems one encounters using a step input, a sample profile is shown in Figure 8.
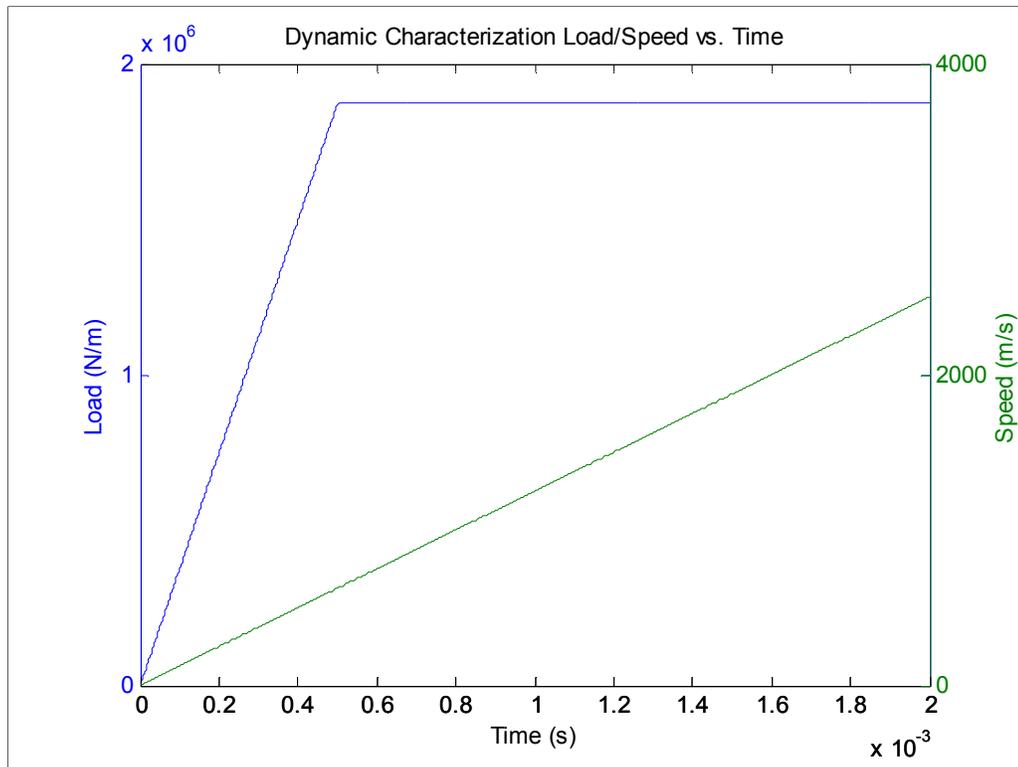
Figure 8: Dynamic Characterization shot profile

By modeling the projectile over a linearly increasing range of velocity values, one can better understand the effect such speeds have on the stresses created within the beam. Though this moving load could also be implemented with a modified railgun shot profile, using the simplified approach reduces simulation setup time and complexity; an advantage over current analysis software.

A modified version of the constant force and constant acceleration load becomes the basis of the Dynamic Load Factor (DLF) analytic tool. For this calculation the acceleration was set to zero and the load was applied across only a portion of the beam with some damping to simulate a statically loaded beam. The DLF is discussed in greater detail in the "Observations/Results" section of this report.

All simulations include short "ramp-up" times of approximately 5ms at the start of the simulation, once again, in order to reduce the errors caused by discretizing the beam and reduce the instantaneous velocities that can cause aliasing and inaccurate results. A value of five milliseconds was chosen to mimic the capacitor discharge rate of the railgun. This duration seemed to noticeably reduce the effects of aliasing while not adding excessive duration to the simulation. Large magnitude, short duration inputs, such as those encountered in electromagnetic launcher create locations of very high displacement velocities which are difficult to approximate with the level of discretization the software is meant for. Reducing special node separation reduces some unrealistic beam behavior though a limit exists where, for this level of analysis, additional computation time does not justify the additional accuracy. An analysis was conducted to determine the correct level of spatial discretization, the chosen amount of nodes for a beam is discussed in the "Model Validation" portion of this report.

3.3   Model Implementation

Implementation of the Timoshenko Beam model into the MATLAB software package for use with the inputs and beam setup discussed in Sections 2.1 and 2.2 requires approximations of the spatial derivatives. These approximations were made using 2nd order finite difference methods.

3.3.1   Finite Difference Approximation

Solutions were calculated by fully discretizing the model in both time and space. The spatial derivatives were approximated using a second order center difference approximation (12) for interior nodes.

$$\frac{\partial w_i}{\partial x} = \frac{(w_{i+1} - w_{i-1})}{2h} \tag{12}$$

Where i is the node index number and h is the spatial separation of the nodes. These techniques were simply applied multiple times when approximating higher order derivatives, yielding equations (13) (14) and (15) for the second, third and fourth center difference spatial derivatives respectively. Boundary differentiations were calculated using the same approximations as the neighboring nodes which reduced discontinuities encountered at the beam ends.

$$\frac{\partial^2 w_i}{\partial x^2} = \frac{(w_{i+1} - 2w_i + w_{i-1})}{h^2} \tag{13}$$

$$\frac{\partial^3 w_i}{\partial x^3} = \frac{(w_{i+2} - 2w_{i+1} + 2w_{i-1} - w_{i-2})}{2h^3} \tag{14}$$

$$\frac{\partial^4 w_i}{\partial x^4} = \frac{(w_{i+2} - 4w_{i+1} + 6w_i - 4w_{i-1} + w_{i-2})}{h^4} \tag{15}$$

Calculation truncation error is reduced by increasing the quantity of nodal elements present in the beam. Using higher order spatial approximations yields more precise results but at the cost of greater complexity. Using the default error settings of the ODE solvers for the temporal discretization, discussed in Section 3.3.2, the implementation of higher order spatial finite difference methods would not yield vastly different results. Strains obtained using Equations (13)-(15) and the default ode45 settings were accurate, see Chapter 5, and it became apparent that correctly identifying an adequate quantity of spatial nodes for a given beam length was of greater consequence and the higher order approximations were not used.

Time derivatives were calculated using the MATLAB ode solver 'ode45' which solves the system of PDEs along a specified time vector; decreasing the time step used until the results fall below a given error level. These levels will be discussed in the following section.

3.3.2 Finite Difference Implementation

   Preliminary iterations of the MATLAB software used user defined time and spatial steps in conjunction with loop structures to calculate beam behavior. This method was computationally intensive and required that the user consider instability issues based on the explicit finite difference scheme used. These issues were relieved, however, when subsequent software iterations implemented the ode solvers within MATLAB.

   Using the spatial derivative approximations, the 4th order non-linear partial differential equation in both spatial and temporal domains was transformed into a 4th order ordinary non-linear differential equation in time. This transformation enabled the use of the efficient and simple to use ode solvers developed within the MATLAB programming environment; the full discretized Timoshenko beam equation for a central node is given by,

$$EJ \frac{\left(w(x_{i+2}, t) - 4w(x_{i+1}, t) + 6w(x_i, t) - 4w(x_{i-1}, t) + w(x_{i-2}, t)\right)}{h^4} -$$

$$\rho J \left(1 + \frac{E}{\kappa G}\right) \frac{\partial^2 \left(w(x_{i+1}, t) - 2w(x_i, t) + w(x_{i-1}, t)\right)}{h^2 \partial t^2} - \tag{16}$$

$$+ \frac{\rho^2 J}{\kappa G} \frac{\partial^4 w(x, t)}{\partial t^4} + \rho A \frac{\partial^2 w(x, t)}{\partial t^2} + k_0 B w(x, t) = P(x, t)$$

   The MATLAB solvers select the time step spacing required to solve the equation based on user defined error tolerances. As with any computational software, there is a minimum time step with which the solvers can use when approximating the solution which depends on the machine precision. For the 64-bit version of MATLAB used this produced a minimum step size on the order of 2.22e-16 seconds. If the user does not specify a sufficient quantity of spatial nodes to meet the tolerances, a minimum time step error occurs and a break occurs as the user is prompted to add more nodes.   This removes some of the stability problems that can occur using a fully discretized solving method.

   The solver used in this software package, ode45, was set to have an absolute tolerance of no more than 1e^{-6} and a relative tolerance of 1e^{-3}. Error is calculated by comparing the product of the solution at a given time and the relative error to the absolute error tolerance, i.e. the error for this solver is set to 0.1% and ignores values lower than 1e^{-6}. These values are easily modified to suit the given problem, should the simulation be excessively long or unstable. Tighter tolerances on the order of 1e^{-8} and 1e^{-5} for the absolute and relative respectively yielded no greater insight into beam behavior when used, though extended computation time considerably.

As shown in Chapter 5, the results generated using the default tolerance values were valid and matched well with experimental data, thus requiring no change.

Each input type and set of boundary conditions uses a modified solver file which requires a different set of variables to be passed in addition to the initial value arrays. Within these files the Timoshenko equation is spatially discretized and the various forcing functions and unique system parameters are defined. This presented a great advantage over the transformation and FE approaches to the problem solution in that the equation never changes form or is hidden from the user. Additions to the model, whether they be damping, non-linear effects due to the armature or even the reduction of the equation to less complex forms such as the Bernoulli-Euler or Rayleigh equations, are easily visualized and implemented. Future iterations of the software will benefit greatly from this design structure.

3.3.3   Stress-Strain Calculations

Stresses within the beam, i.e. shear and bending, are calculated using their spatial derivative approximations of the displacement, as given in Shigley's Mechanical Engineering Design [8]. The bending moment is proportional to the second derivative of displacement with respect to x, the modulus of elasticity of the beam and its second moment of area about the neutral axis, Figure 3, with this the bending stress is calculated using (17) and (18).

$$M(x) = EI \frac{\partial^2 w(x,t)}{\partial x^2} \tag{17}$$

$$\sigma_b = \frac{M(x)y}{I} \tag{18}$$

Where $M(x)$ is the bending moment, σ_b is the bending stress and y is the distance from the beam centerline to the beam surface or half of the beam height. The outer most surface would thus be the point of greatest bending stress and strain. It is for this reason that all strain and bending stress plots and values, with the exception of the von Mises plots, are given for the outer surface. This was done for ease of comparison between experimental data and modeled data. For a better analysis of stresses within the beam the shear values were also calculated.

Shear force is defined as the third derivative of deflection with respect to space and obtained using equation (19). For a beam in bending, the shear stress is given as a function of the shear force imparted by the load, the second moment of area about the beam's neutral axis, and the position of the element in relation to the center line. For a rectangular beam the stress due to shear is given by (20).

$$V(x) = EI \frac{\partial^3 w(x,t)}{\partial x^3} \tag{19}$$

$$\tau(x) = \frac{V}{2I}(c^2 - y^2) \tag{20}$$

Where V is the shear force due to the applied load and the variables I, c, and y are the second moment, distance to the beam surface, and distance from the neutral axis once again. From basic design theory, the greatest shear stress occurs where the bending stress is zero, i.e. the neutral axis. This value is given by (21) and is used in all shear stress and DLF shear plots except the von Mises calculations which use the more generalized equation.

$$\tau_{max}(x) = \frac{3V}{2A} \tag{21}$$

The Distortion Energy Theory (DET), also referred to as the von Mises theory, plane stress calculations were included for the use in beam design and analysis. The beam experiences tensile and compressive stresses normal to the cross-sectional area in addition to shear stresses parallel to the cross-sectional area. Plane stress within the beam is calculated by combining Equations (18) and (20) into the von Mises equation (22),

$$\sigma' = \sqrt{\sigma_x^2 + 3\tau_{xy}^2} \tag{22}$$

Though von Mises calculations also include the stresses due to forces normal to the beam surfaces, distortion due to these forces is negligible in comparison to bending and shear and has been removed.

Bending strains were calculated using *Hooke's Law,* Equation 23, relating the bending stress, modulus of elasticity and strain.

$$\epsilon_b = \frac{\sigma_b}{E} \tag{23}$$

This is valid only over the linearly elastic region of beam loading which, as shown in later sections, is not always the case during weapon launches.

3.4   Wave Velocities

Wave velocities within the beam, and the importance of these waves during a projectile launch, are a key focal point for this software package. Wave energy travels down the rail at one of two velocities defined by the method by which it is transferred within the rail,

bar(compression) or shear, given in (24) and (25) respectively. The bar velocity represents physical limit that waves, i.e. energy, can travel within the beam.

$$v_b = \sqrt{\frac{E}{\rho}} \tag{24}$$

$$v_s = \sqrt{\frac{\kappa G}{\rho}} \tag{25}$$

A third velocity, which describes the minimum velocity required to generate unattenuated beam displacement ahead of the projectile, is known as the critical velocity (26). Unlike, the bar and shear wave speeds, the critical velocity is a function of both beam and beam containment quantities, namely the containment stiffness.

$$v_{cr} = \sqrt[4]{\frac{4k_0 BEI}{\rho^2 A^2}} \tag{26}$$

Equation (26) is an approximation of the beam critical velocity based on the more specific Bernoulli-Euler model though as indicated in [1] it is within a few percent of the Timoshenko value and is much more intuitive. Design of a system at this level does not require the exact critical velocity but instead a close approximation, thus the Bernoulli-Euler approximation was sufficient.

Beam displacement behavior is expected to undergo significant transformations as the load is applied traveling down the beam at the various velocities. As illustrated in this document, beam displacement does in fact change shape as the projectile accelerates, i.e. pre/post critical and pre/post shear velocity regimes. Typical wave speeds for a small scale experimental railgun are listed in Table 4; these velocities are within the same order of magnitude as the traveling load which causes a variety of interference effects, all of which are harmful to the rail bore life. Through the use of the wave speed equations and simulation software such as the proposed MATLAB software, the system can be modified to provide more desirable beam behavior over the range of speeds it will be operating.

Chapter 4: Applied Timoshenko Model

The Timoshenko model was applied to a beam: convergence, visual inspection, and accuracy as it is compared to known beam response data. It will be shown that all three are successful tests and indicate a valid simulation. Table 3 lists the system parameters used in the model convergence and accuracy simulations, with the exception being the infinite beam case used in 4.1.2 in which the beam length was extended to 8m.

Table 3: System Simulation Parameters

Parameter	Value
Beam Length	1.5456 m
Beam Height	0.01 m
Beam Width	0.019 m
Modulus of Elasticity (Beam)	120 GPa
Damping	20000 N-s/m
Cross-Sectional Moment	1.583×10^{-9}
Beam Material Density	8320 kg/m^3
Foundation Stiffness	7.89×10^{10} N/m^3
Shear Modulus	45 GPa

4.1 Displacement Shape Analysis

Upon applying the Timoshenko model to the system described in Table 3, the first test of model validity was an analysis of the beam behavior under the various loading methods and speeds. Steps for setting up and running these simulations are outlined in Appendix A.

4.1.1 Impulse Test

The first test for a valid model entailed a simple analysis of the beam behavior as it was loaded. Two input types were used: impulse and accelerating. The impulse test was meant to show the proper beam behavior and wave propagation away from the load location, in this case, near the center of the beam at 0.7m, as shown in Figure 9.
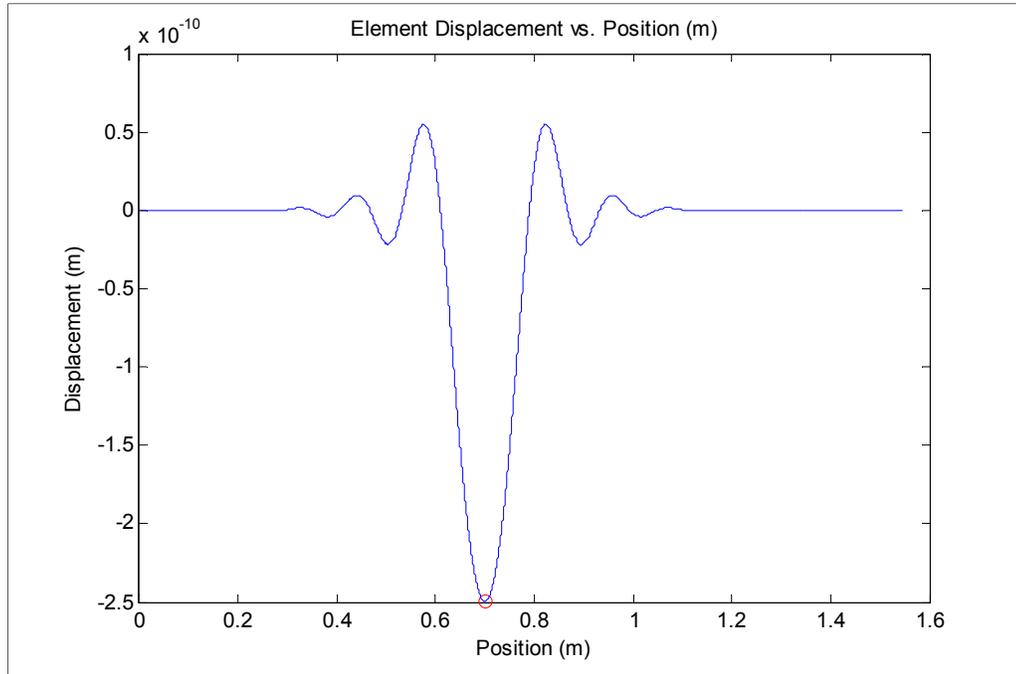
Figure 9: Beam Response to Impulse Load

For this simulation, which ran for 0.003 seconds, also illustrates the ability of the model to match beam velocities, such as the shear wave. The plot in Figure 10 is a snapshot of the beam displacement at 0.0018 seconds; this indicates that the beam had been excited for approximately 0.3ms in which time one would expect a wave traveling at approximately 2325 m/s to move 0.6975m. After further analysis of the plot there was in fact beam displacement around 1.4m as predicted thus confirming the energy transfer capabilities of the Timoshenko model and accuracy of the wave velocity equations.
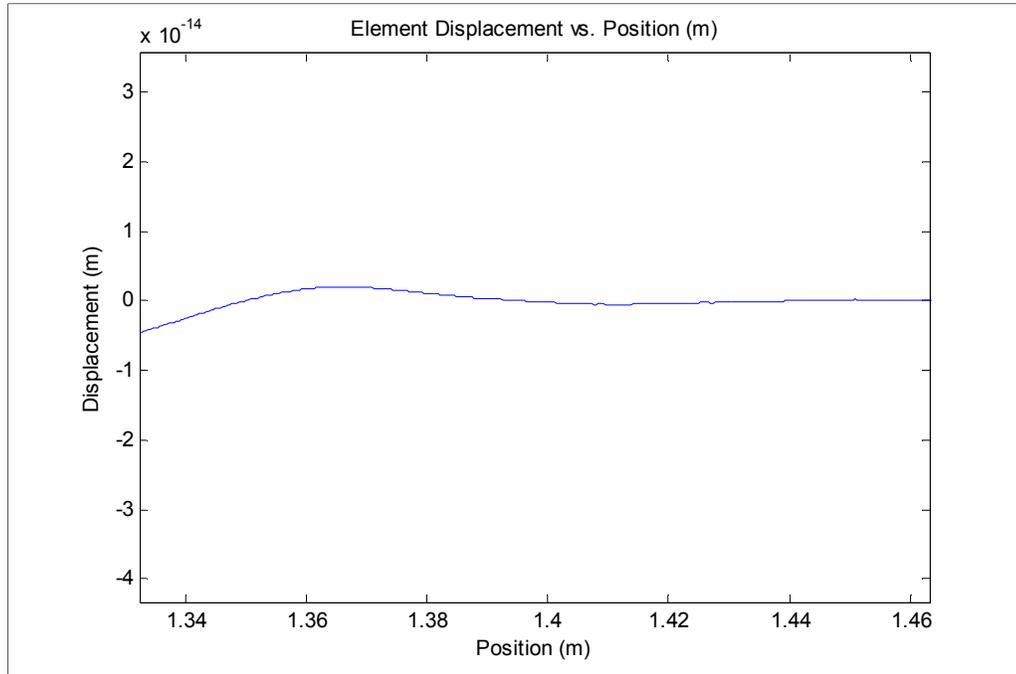
Figure 10: Beam Displacement due to shear wave propagation

Also of interest were the boundary responses, namely free-free or pinned-pinned. The free boundary is the more realistic of the two though both were tested and performed as expected. The pinned-pinned boundaries produced no displacement and inverted the traveling waves as they reflected off the ends of the beam. The free ends were non-inverting and produced beam displacement without a bending moment or shear forces, except for the moving load case where shear exists while the load is concentrated on this point.

4.1.2   Traveling Point-Load Test

The traveling load simulation required a more rigorous analysis to ensure the correct beam behavior over a wide range of velocities. The response of an infinite beam on an elastic foundation is well documented using FEA techniques [1] and by Fryba's analytical approach [2]. For each simulation, an 8m beam was used consisting of 5000 spatial nodes to approximate an infinite beam. Table 4 lists the three beam velocities; beam behavior is expected to transition when the projectile reaches new velocity regimes. These regimes are identified as pre-critical, post-critical/pre-shear, and post-shear. The displacement shape after the shear wave velocity remains similar for greater speeds.

Table 4: System Beam Velocities

Velocity	Velocity
Bar (Compression) Wave	3797.77 m/s
Shear Wave	2325.65 m/s
Critical (Beam)	821.72 m/s

Below the critical velocity, the point of greatest displacement coincides with the location of the load, indicated in Figure 11 by a red circle. This response is similar to that of a statically loaded beam, as shown by Johnson and Moon [1]. The FD model shown below closely matches their ANSYS model, though like their model, displays acceptable levels of discrepancy compared to the analytic model. Comparisons to the ANSYS and analytical models are made qualitatively and not quantitatively based on beam behavior within this velocity region.
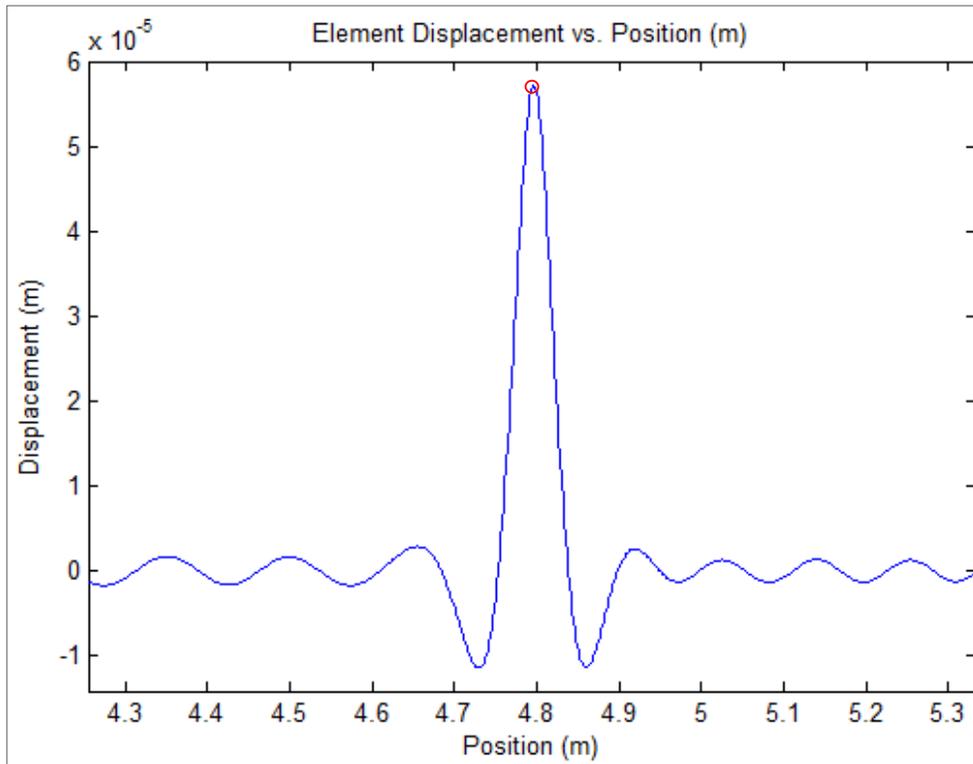
Figure 11: Displacement plot for a load traversing the beam below the critical velocity

A second simulation modeled the load velocity at 1200 m/s, which is within the post-critical/pre-shear velocity regime. When the load reaches this speed waves which propagate outward from the point load do not attenuate, Fryba[2]. Figure 12 shows the location of the point load as a circle, it is important to notice the location of the maximum displacement shifts from the location of the point load to behind the projectile location as the load begins to rise out of the

deflection well. While loads traveling at speeds below the critical velocity produce similar displacement magnitudes as those indicated in Figure 11, the difference is in the displacement away from the load caused by the unattenuated traveling waves. Greater deflections and stresses are shown over greater portions of the beam when compared to the low velocity case.
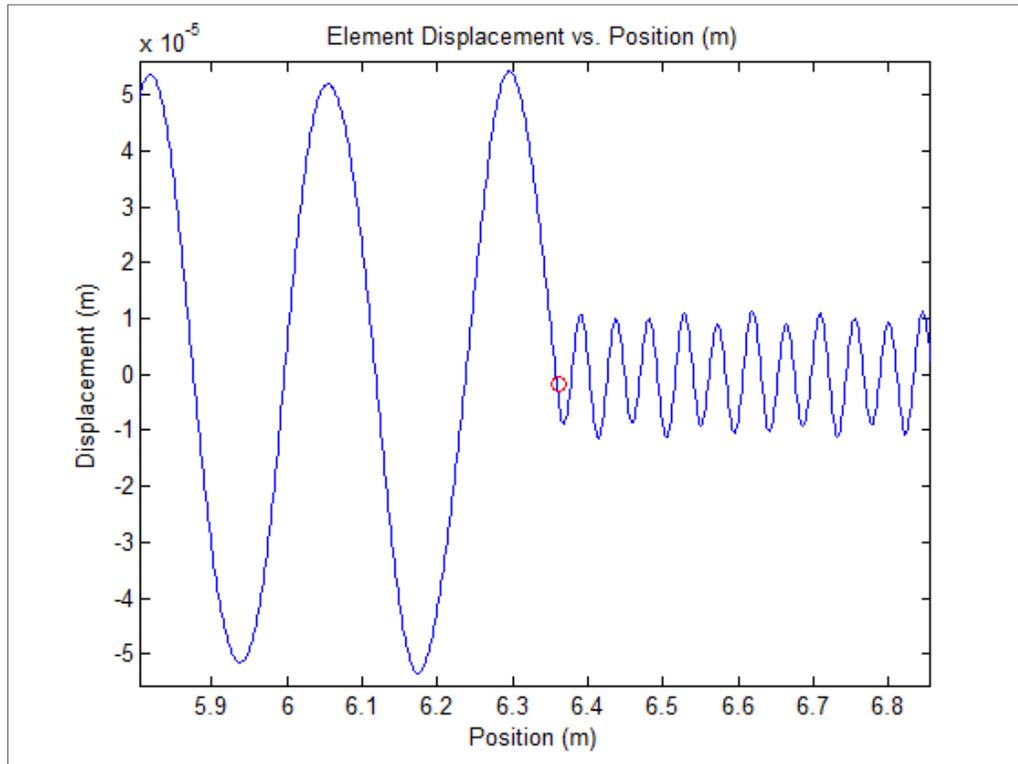
Figure 12: Displacement plot for a load traversing a beam between critical and shear velocities

It will be shown that for an accelerating load the projectile begins to "catch up" to and pass the waves previously emitted, creating the plot shown in Figure 13, depicting a load traveling at a constant 3000m/s. The load has now surpassed the shear wave velocity; waves propagating ahead of the load are greatly attenuated and produce almost no deflection. For speeds greater than the bar velocity the beam is unable to transfer wave energy faster than the movement of the projectile thus no beam deflection occurs ahead of the moving load. Also important to note is the reduced beam displacement and much lower frequency waves behind the load as compared to the moderate velocity case. The stresses experienced by the beam when traversed at this velocity are greatly reduced compared to the lower velocity test cases. This is of great importance for future rail designs in which containment materials around the rail may be changed depending on the anticipated beam response and projectile velocity at that location.
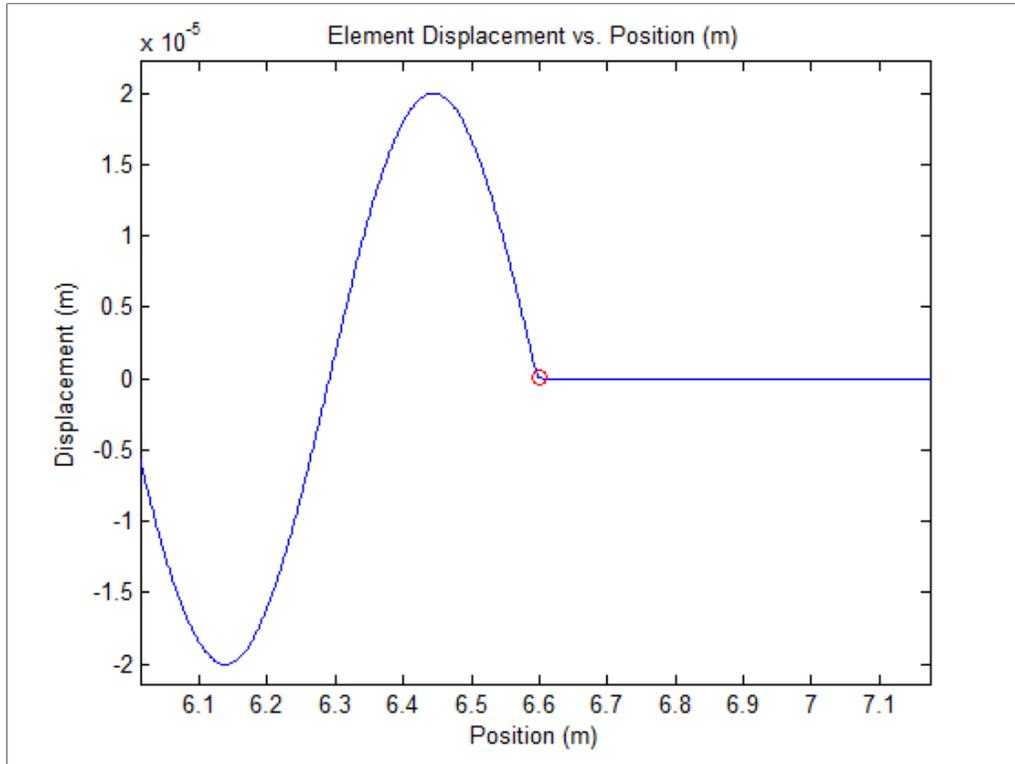
Figure 13: Displacement plot for load traversing a beam at greater than shear wave velocity

All three simulations produced beam behavior results in agreement with previous research within the field and served to validate the FD model in its ability to precisely model the Timoshenko beam and the various established beam transition velocities.

4.2   Model Convergence

The shortest traveling wave wavelengths were found to be similar in scale to beam dimensions, around 0.05 m in length. In order to adequately represent these characteristics requires the spatial discretization to be 0.025 m or 2 nodes per waveform. This is an absolute minimum to crudely visualize the beam displacement behavior. Using fewer nodes predicts increasingly erroneous results which offer nothing to the researcher. While beam displacement behavior can roughly approximated by using very low node quantities the stress and strain characteristics cannot. Stress and strain values are calculated using finite difference approximations of spatial derivatives, see section 3.3, and as such require far more nodes to accurately predict. An important component of the finite-difference approach is the balance of model accuracy and computation time. Following an analysis of model convergence it became apparent that the accurate and precise simulation of the beam/rail during launch did indeed require significantly more nodes per waveform, approximately 130. This value was selected after comparing a large range of node quantities.

28

Simulations for an undamped 1.5456m beam with railgun loading were per run with 1000, 3000, and 8000 spatial nodes. From these tests the need for over discretization of the beam was not justified, instead, barring some undesirable oscillation behavior brought about by damping, the 1000 node case did not yield vastly different results from that of the much more computationally intensive 8000 node case. The plot in Figure 14 shows this relationship for a period of time at 0.5m. This location on the beam was chosen to illustrate the beam strain after peak current and the critical velocity have been reached so as to incorporate wave interaction and armature velocity transitional effects. Peak strains at this location were nearly identical and wave shapes are shifted slightly as a result of spatial rounding errors between the three.
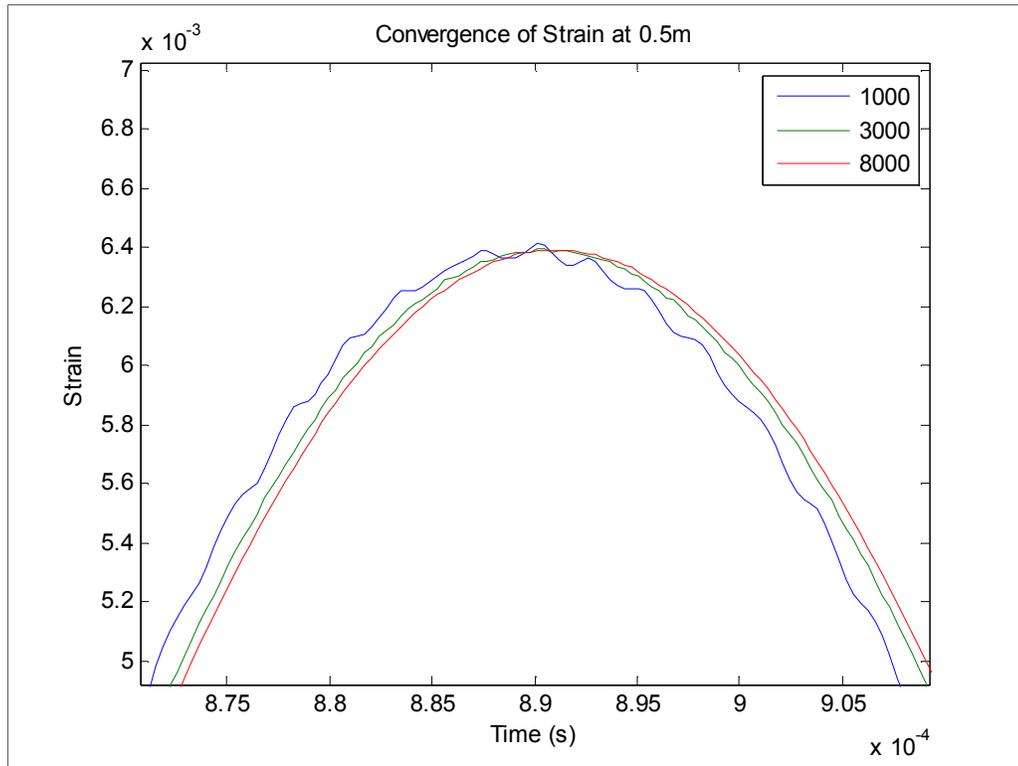
Figure 14: Strain convergence at 0.5m for 1000, 3000, and 8000 spatial nodes

The results of Figure 14 were over optimistic, however, as additional effects were incorporated into the model, especially when damping was included. Figure 15 once again shows the same beam location strain curve during launch. As one can see, the addition of damping caused the 1000 node spatial node case to become unstable and predict inaccurate, unnatural behaviors. This is largely due to the approximation of both the spatial and temporal derivatives. With the low number of beam elements the spatial derivatives are inaccurate and unable to correctly predict beam behavior throughout the launch. Deriving strain from spatial derivatives (17), (18) and (23) becomes more accurate as the space between nodes becomes infinitesimal and the error encountered when approximating using the finite difference methods is reduced.
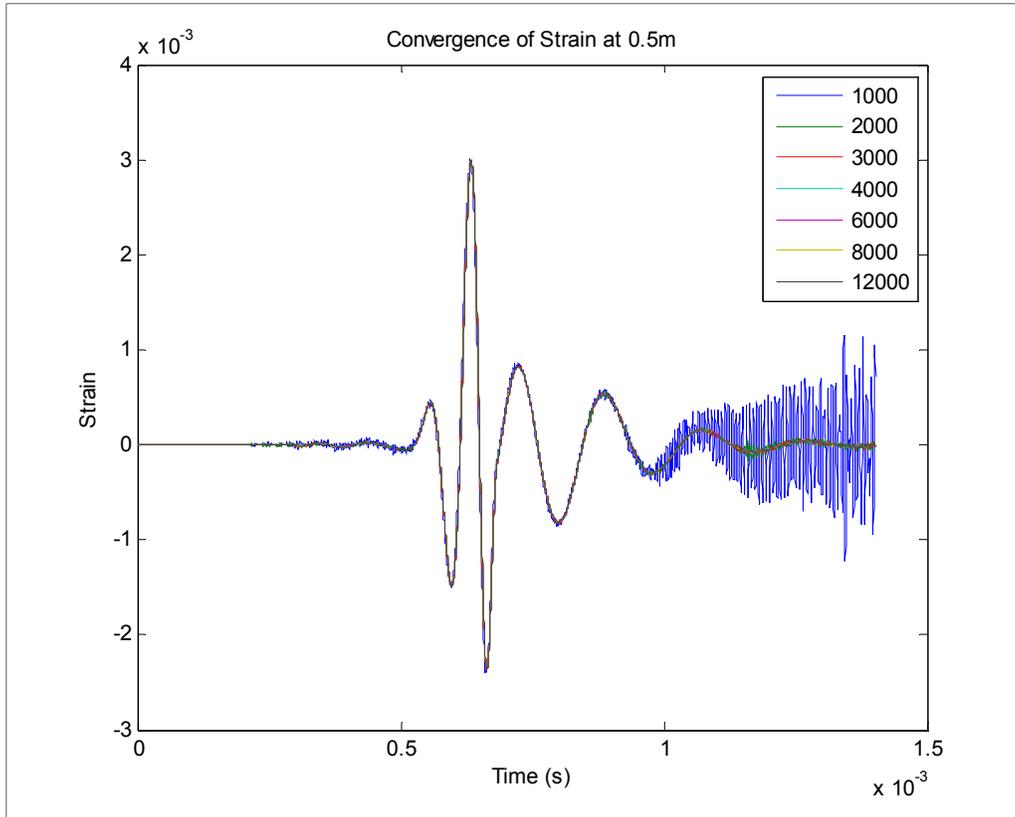
Figure 15: Convergence Plot for 1000-12000 spatial nodes, 4000 temporal nodes

During the period of time where the armature passes, around 0.7ms, even the low node count case still predicts the beam shape quite well. By increasing the number of elements the instability is reduced and the results quickly converge. These cases, however, still have significant oscillations when compared to even higher node count cases. Figure 16 gives a closer look at this phenomenon, in order to simplify the plot the 1000 node case has been removed, as one can see there is a significant reduction in predicted beam oscillation from 3000 to 4000 nodes. This can be seen again in Figure 18 with the maximum strain experienced. The smaller distances between the calculated nodes, approximately $3.9*10^{-4}$ m, inherently makes the second order finite difference approximations more accurate. Though the level of accuracy for this analysis is also balanced heavily with the computation time required, the 1000-3000 cases are not acceptable. A simulation with greater than 4000 nodes is nearly required for this beam length with 6000-8000 node cases being used for a more uniform plot, refer once again to Figure 16.
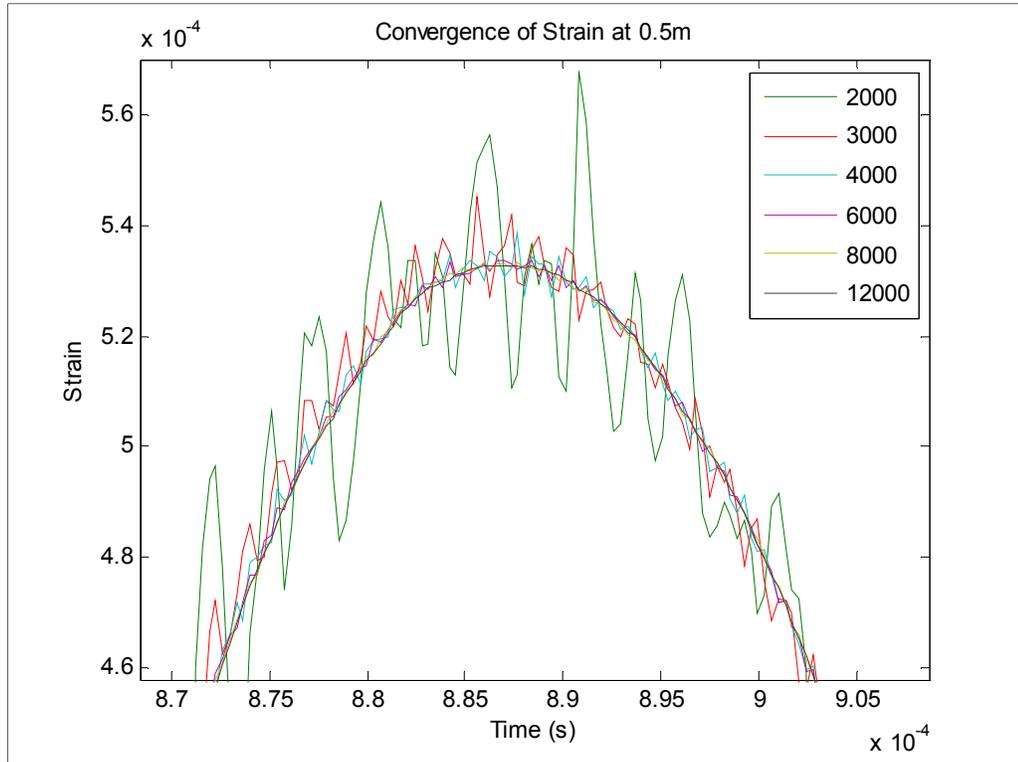
Figure 16: Enlarged plot of model convergence

Figure 17 shows the strain variance at 0.5m for the same railgun simulated launch. This plot quantifies the oscillations seen in Figures 13-15. The 1000 and 2000 spatial node simulations varied wildly at times when compared to the more computationally intensive cases, and while the 3000 node beam oscillated far less than these lower cases, it too was determined to be to imprecise for use.

Figure 18 shows a different convergence plot, focusing on the maximum calculated bending strain experienced by the rail over all space and time steps. The maximum strain value, though it occurs for a short period of the projectile launch, is an important design parameter and has served as a good comparison value between simulations. One can see that using greater than 3000 spatial nodes yields almost no greater accuracy in calculating the largest strain while values below 3000 nodes produce increasingly erroneous results. From the analysis of Figures 13-17, it was concluded that a conservative value of 4000 spatial nodes was an acceptable compromise of system computation requirements and accuracy/precision.
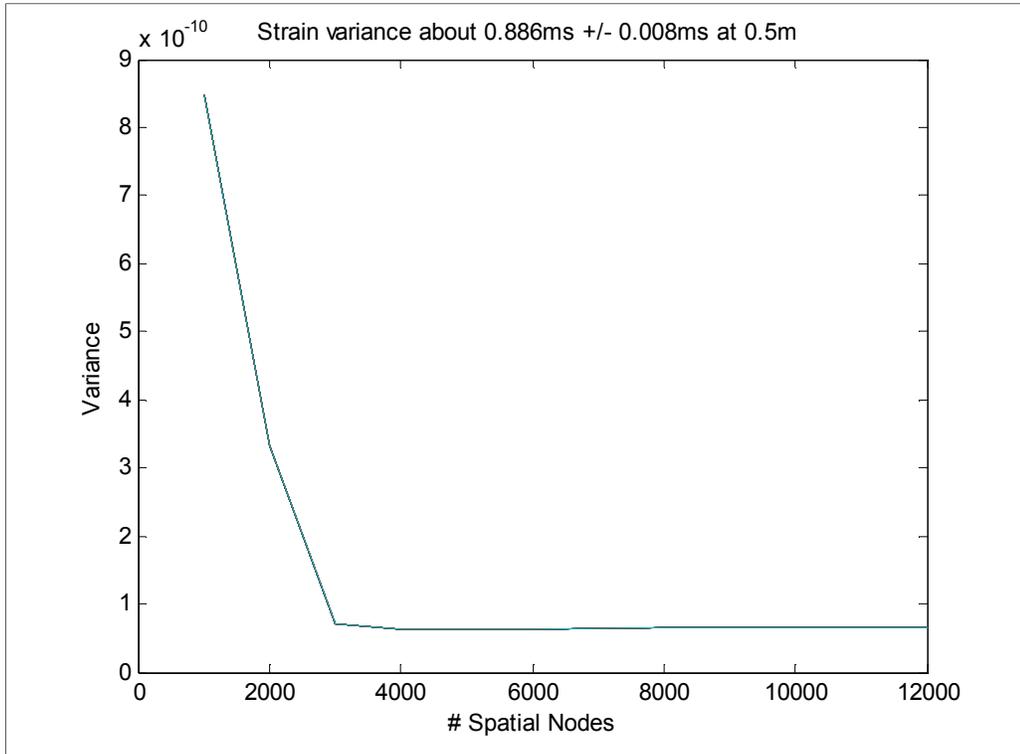
**Figure 17:** Strain Variance at 0.5m for 1000-12000 spatial nodes
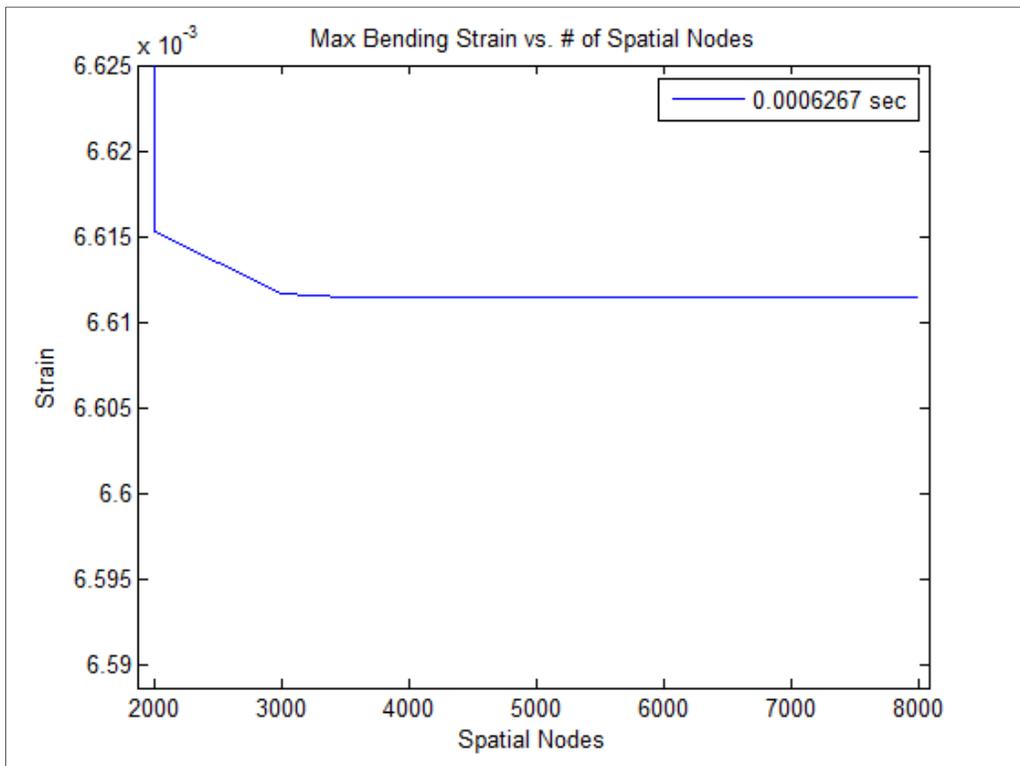
Figure 18: Convergence of maximum bending strain experienced by beam

While 4000 spatial nodes accurately characterizes a 1.5456 m beam with separation of approximately $3.9*10^{-4}$ m it was necessary to conduct a second set of simulations to confirm that a similar quantity could also define a new beam design. For the new setup the beam shape and containment were set to identical values as the original while beam length and loading were changed. The dynamic characterization input was applied, using a load initially traveling 750 m/s which accelerates to 1500 m/s along the 1 m beam. Figure 19 indicates that the maximum strain experienced once again converges when node separation approaches $3.9*10^{-4}$ m which corresponds to 2500 to 3000 nodes. Thus for future analysis it is recommended that each meter of beam length be approximated by greater than 2500 spatial nodes. Rough beam behavior results are obtained using quantities lower than this when speed or system resources dictate their use.
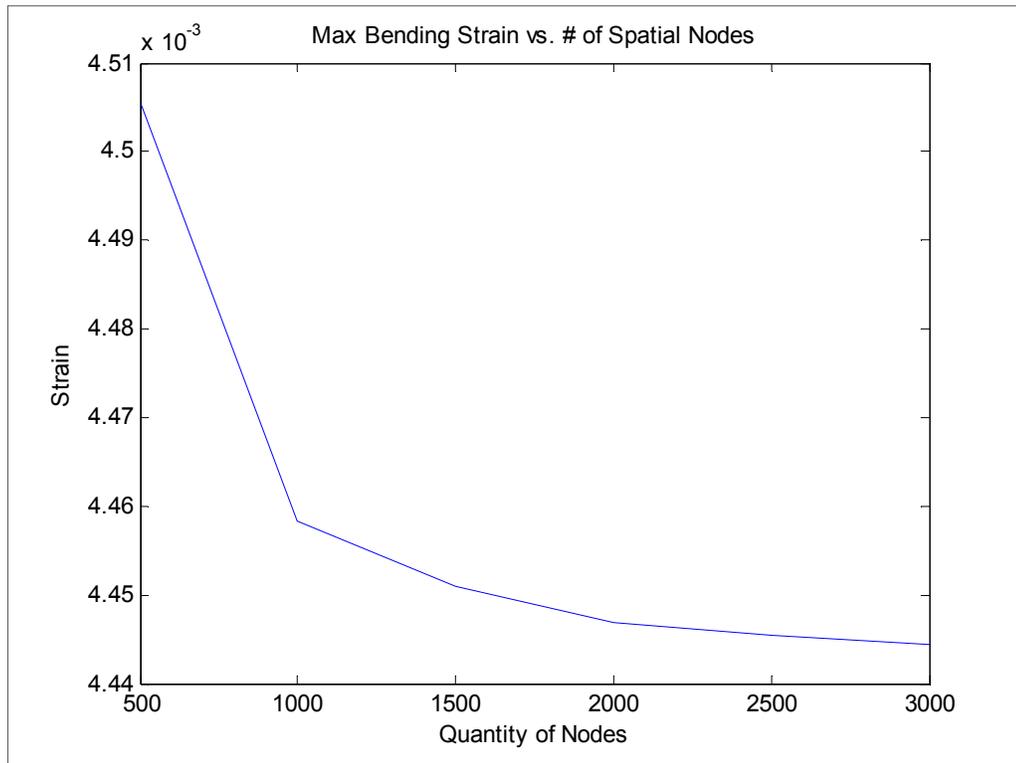
Figure 19: Convergence of maximum bending strain

The algorithms implemented by the ordinary differential equation solver used, ode45 in this case, determine the appropriate time step in order to meet accuracy tolerances for each location in the time array, as set by the user. For this reason large time vectors, though they provide a smoother plot, have a minimal effect on the computation time, efficiency, or model accuracy. The choice to use 4000 data points for the simulations in this report was a conclusion developed based on the convergence results as well as computation time and memory considerations. This software package was created to be used on a wide range of computing platforms, from mobile laptops to high end desk models, thus the ability to adjust the size of the time step array is still part of the front end user interface and can be changed to fit the user's computational limitations.

Chapter 5: Railgun Finite Difference Validation

5.1   Experimental Strain Gauge Comparison

Declassified electromagnetic launch data was provided for the purpose of validating the strain analysis capabilities of this software. The comparison of the experimental data and simulation output has served as an indicator of the FD approach's ability to match not only beam behavior over a range of velocities but also deflection and strain magnitudes.

Strain gauge data was given for four locations along the rail; two are presented below, 0.5m and 1.3m. Discrepancies between the base measurement location on the test apparatus and the armature have created a 0.17m difference in the gauge location and simulation location, when this distance is taken into account the plots coincided very well.

A plot of the 0.5m strain gauge data is shown in Figure 20. The gauges measured beam strain values up to 5000 µɛ at the beam surface opposite that of the projectile. As shown in the figure, the strains endured well exceeded the 5000 µɛ maximum thus causing the values to be clipped several times. This prevented an exact comparison of the simulation to the experiment, though, as Figure 21 shows, the simulation does coincide with the simulation and indicates a very strong correlation between the two.
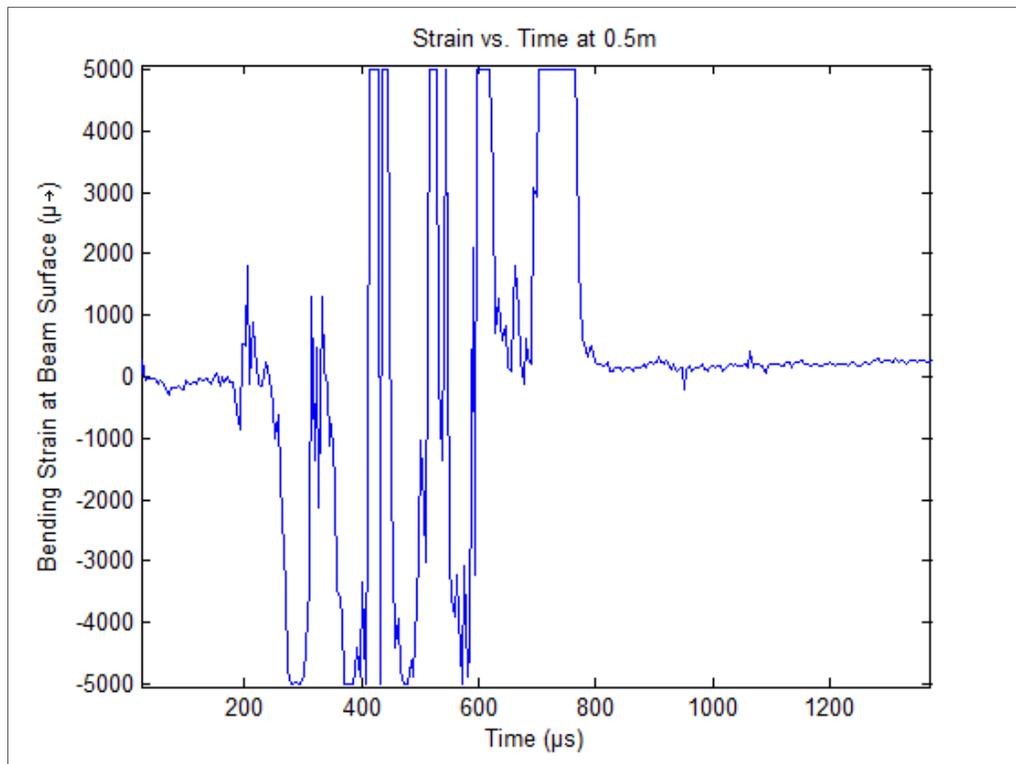

Figure 20: Experimental Strain data from beam surface at 0.5m

The beam response approximated by the FD method shows a similar beam shape before and after the load passes. First, small perturbations are present due to the faster moving shear, beam and pressure waves that propagate ahead of the load. The load then reaches the beam element, causing the large positive tensile strain values seen around 5ms. These values are of the same order of magnitude and appear to be very close to the actual strains seen during the test fire, within approximately 10-15% of the experimental values. Adding damping to this model causes the displacement, and so the strains, to attenuate as the load moves farther down the rail. It is apparent that the damping present within the actual experimental setup is larger than that included in the simulation, though the simulation is limited in the amount of damping it can include due to the errors incurred during discretization of the beam and boundary condition approximations.
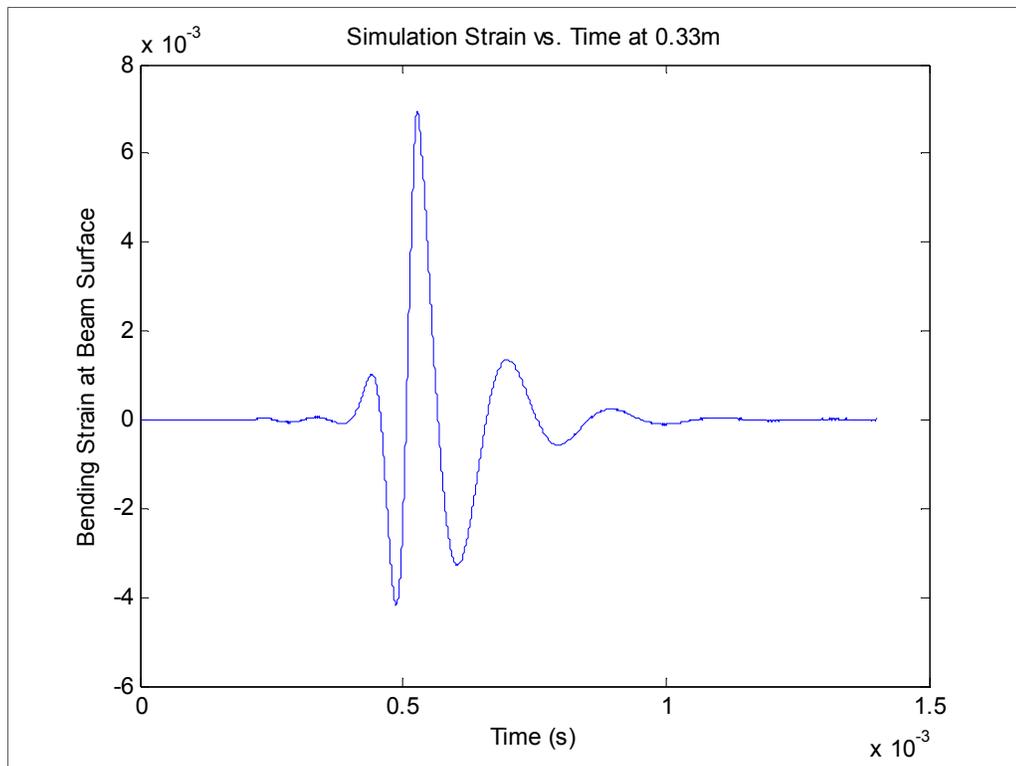
Figure 21: Simulation Bending Strain at 0.33m

An additional plot is shown in Figure 22 for a location closer to the end of the beam, 1.3m or approximately 1.13m using the software. From the graph one can see that the strains experienced this far down the beam are an order of magnitude less than those seen closer to the breach, which is due to a combination of several things. The current at this time, about 1.1ms, is much lower than at the 0.5ms case shown in Figure 20. Additionally, the velocity transitional effects are no longer present; the projectile has entered the post-critical/pre-shear velocity regime and is no longer accelerating at an appreciable rate.
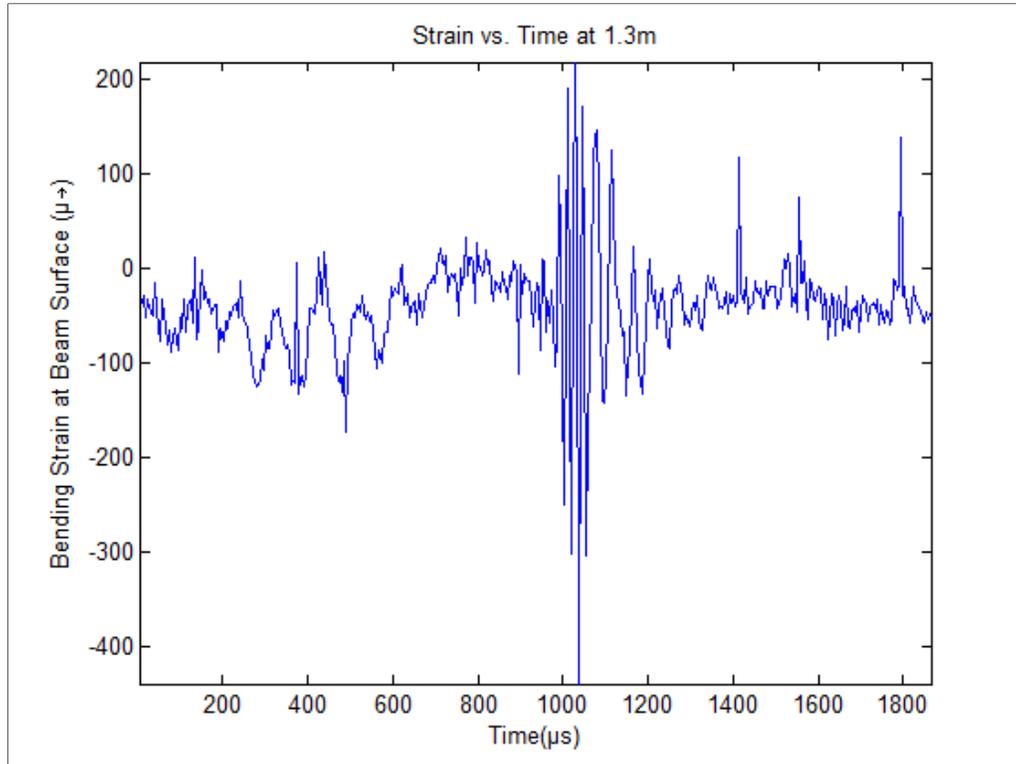
Figure 22: Experimental Strain data from beam surface at 1.3m

The MATLAB simulation results are shown in Figure 23. This simulation was run with a damping coefficient of 20000 N-sm^{-2} which reduced the strains seen during launch; a comparison of a damped to undamped beam is given in Figure 24 at 0.05m. The displacement plot begins to closely match the current profile when damping is included, this is more indicative of the beam behavior expected when a projectile is fired, removing the large sinusoidal behaviors seen during an undamped test case. While the inclusion of damping enhanced the shape and amplitude of beam strain values, it is apparent from these simulations that the use of additional components could generate more accurate results. From Figure 23 one can see that the simulation still matches Figure 22 quite well. Small strains are predicted prior to the load application where the higher velocity shear, beam and pressure waves cause small displacements.
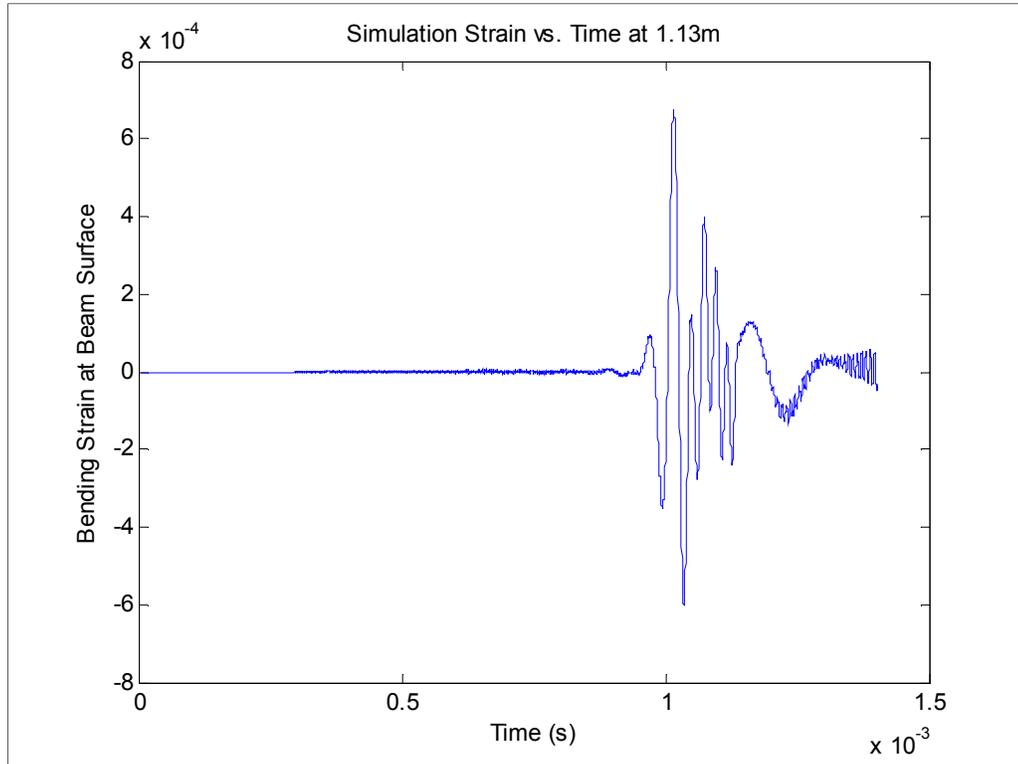
Figure 23: Simulation strain results for the surface of the beam at 1.13m
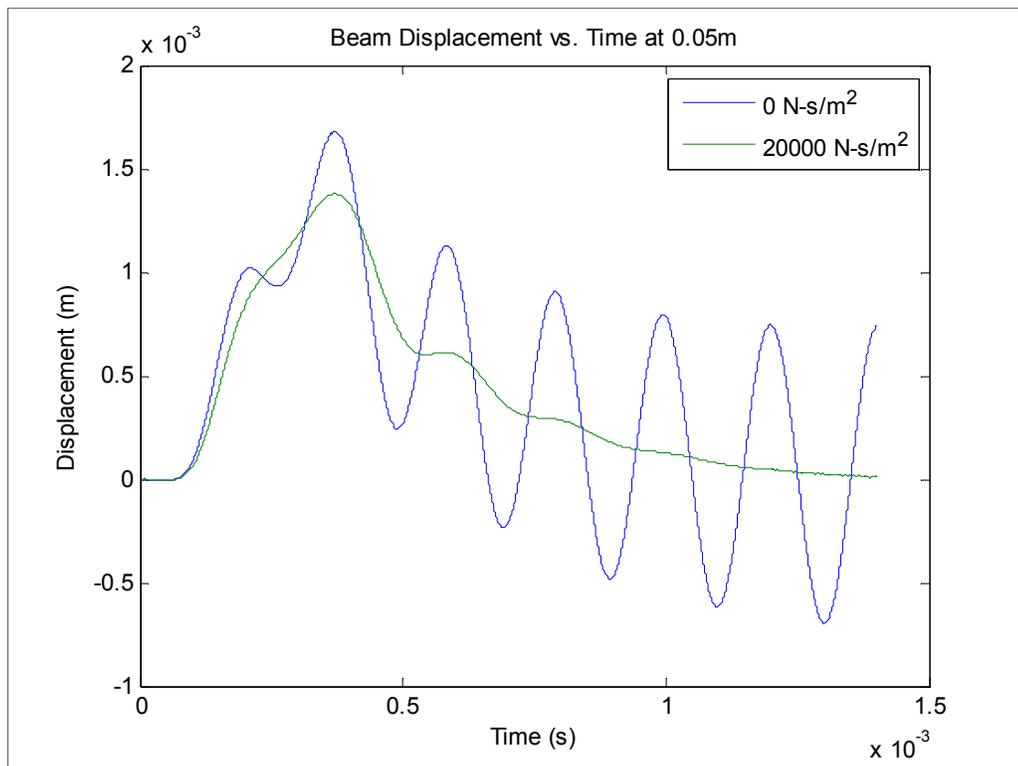
Figure 24: Effect of damping on beam response during launch at 0.05m

As with the previous plot, high frequency bending of the beam is not matched by the model, however the strain magnitudes are well defined and illustrate a clear relation between the Timoshenko model and the experimental tests. The model over predicts the maximum surface bending strain by approximately 35%; though as discussed, it is during this length of the beam that many non-linear effects such as arcing and armature skipping occur which have yet to be defined within this software package. These effects are known to cause uneven pressure peaks along the armature during and after transition occurs though their effect on the beam, specifically for this setup, have not been defined. This is yet another aspect to be covered in future railgun research when additional, more detailed, experimental data can be incorporated.

5.1.1   Experimental and Simulation Strain Correlation

While Figure 23 indicates that the FD model can accurately predict maximum strain values as compared to a strain gauge 0.5m down rail, which corresponds to a location which experiences high current values, it is also important to quantify the correlation of the predicted strain to experimental strain. A plot of simulation strain and experimental strain at 1.3m down rail is given in Figure 25. Both gauges indicate that the beam is initially strained prior to the application of a load, which is not predicted by the software model. However, from the figure one can see that under loading the strains predicted by the simulation are once again similar in magnitude and form to those seen during testing. The loading and wave interaction conditions are vastly different at this time and location when compared to those at 0.5m. Currents are much lower and the various traveling waves have now had sufficient time to propagate and reflect multiple times; successful modeling under these conditions is required for a valid simulation package.
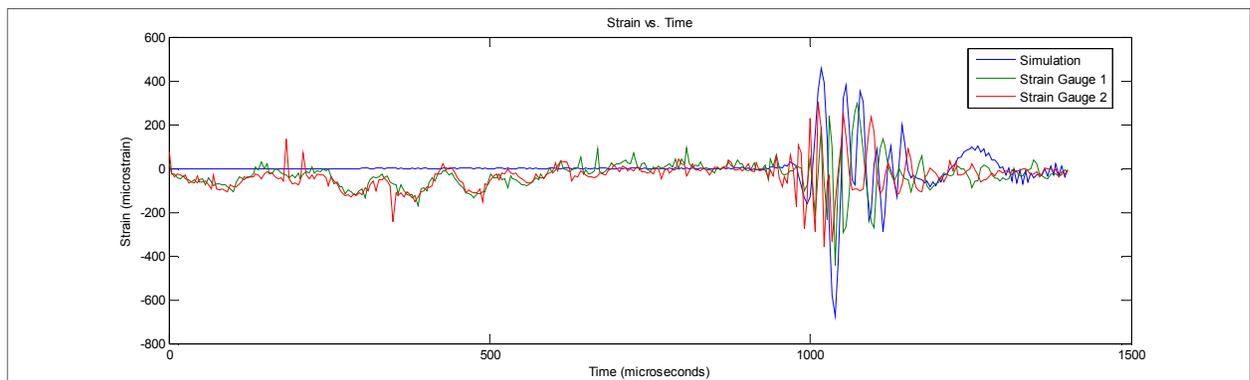

Figure 25: Simulation and experimental strain vs. time

The normalized unbiased cross correlation between the simulation and experimental data is shown in Figure 26. There is an obvious correlation between the two around zero tau, or no lags.

The spike in correlation at these locations is due to the similarity in strain magnitude and shape though the experimental and simulations do not match perfectly partially due to armature location discrepancies between the model and test setup, signal noise, and the simplicity of the Timoshenko beam model used. The level of complex behavior the rail displays during launch is beyond that of the 1-D Timoshenko beam, as the Timoshenko model only incorporates bending strain at the rail surface while the experimental beam strain is a combination of several components including bending, longitudinal, and torsion effects. The purpose of this model is to simply approximate these effects and as such some disagreement within the cross correlation and strain data does occur. The two signals are increasingly uncorrelated for tau values away from zero.
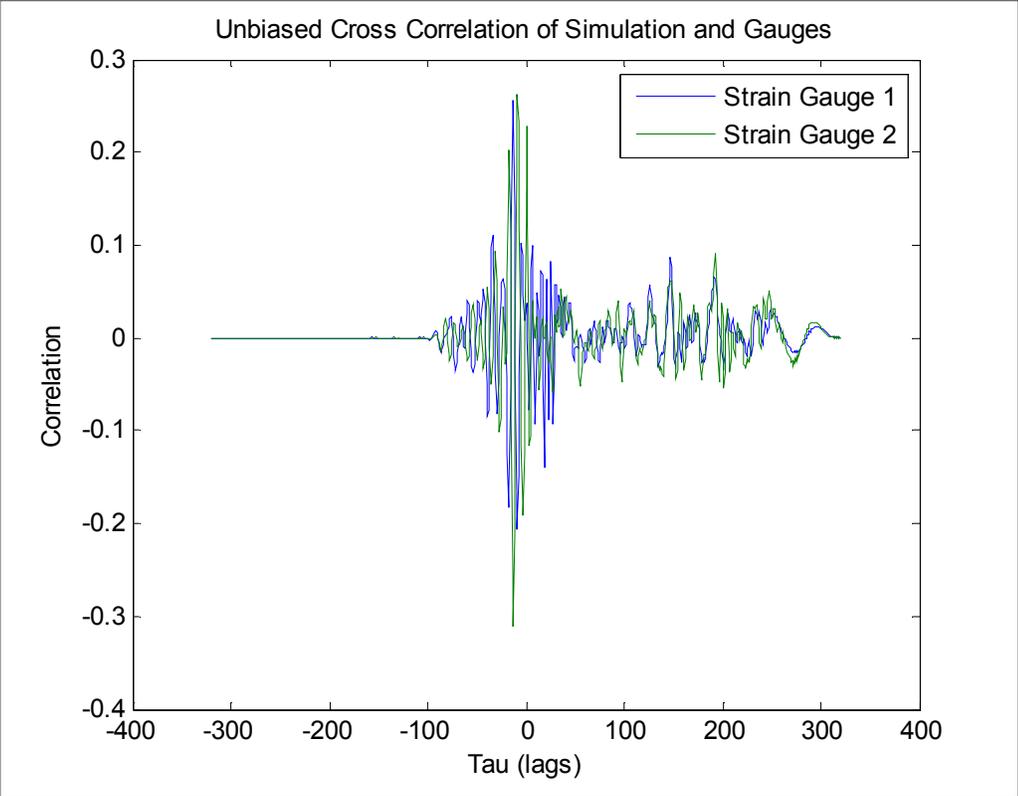
Figure 26: Normalized cross correlation of simulation and gauges

Finally, a cross-spectrum analysis was used to compare the frequency content of the simulation of the gauges. Figure 27 displays the results of this analysis. The teal plot indicates the cross-spectrum of the FD model to the gauge and, for comparison, the red displays that of two gauges. Similar spectral forms are evident, especially in the lower frequency range, around 5000-45000 Hz. The high frequency limitations of the model are visualized, however, for frequencies in the 45000-70000 Hz range. There is a large portion of frequency content shared by the two gauges which is not present in the simulation. This is also seen when reviewing

Figure 25, it is obvious that the Timoshenko model simply cannot match the high frequency behavior seen during the experimental launch.
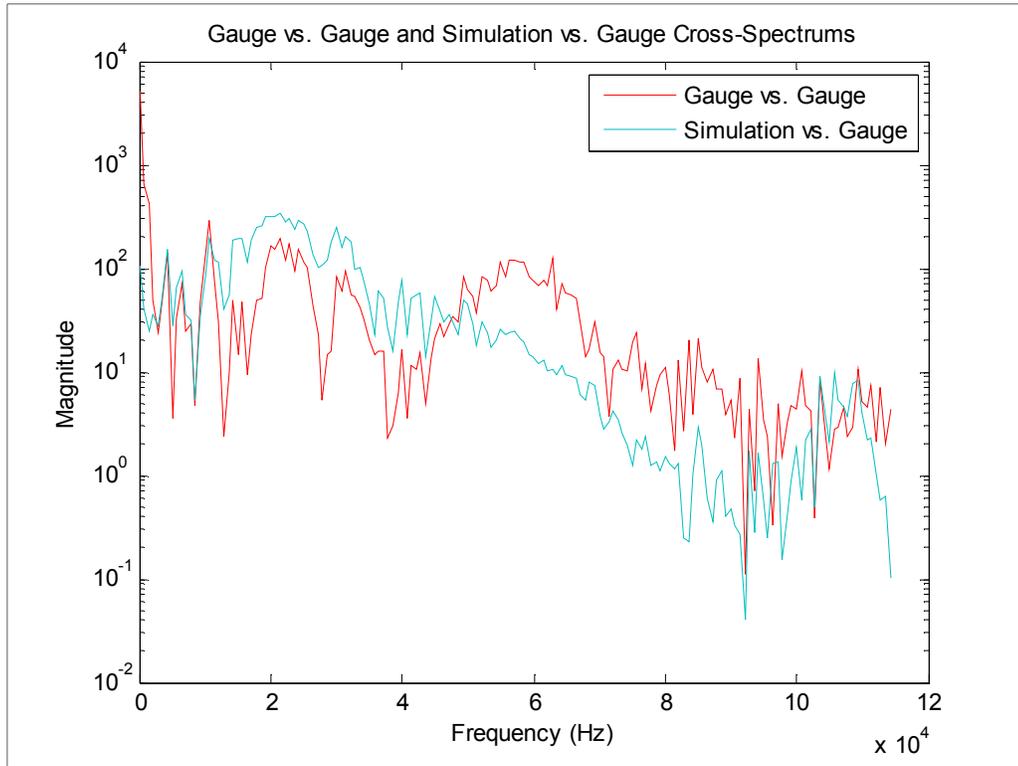
Figure 27: Cross-spectrum analysis of strain gauges and simulation

The Timoshenko model's ability to correlate adequately with experimental data and simulate rail behavior over a similar range of frequencies validates its use for preliminary design review, despite some inaccuracies and limitations.

5.2   Computation Time

The computation time required for these simulations was a concern when developing this software; however, for the level of accuracy, they were quite low when compared to traditional FEA solvers. Analysis of the computation time for various node combinations is shown in Figure 28. The simulations were calculated using 64-bit Matlab 7.11.0 (R2010b) running on an Intel i7 CPU 860 listed at 2.79 GHz with 16GB of RAM. It is recommended for large simulations, those greater than approximately 2m, that a 64-bit version of MATLAB be used in order to handle the large data arrays created. From the convergence test, Figure 14 through Figure 18, one can infer that the 8000 and 12000 node cases are both excessive levels of discretization, though the solver still only requires 1500 seconds, or approximately 26 minutes.

Using 4000 spatial nodes is more indicative of normal program use and requires only 473 seconds (less than 8 minutes) of computation time.
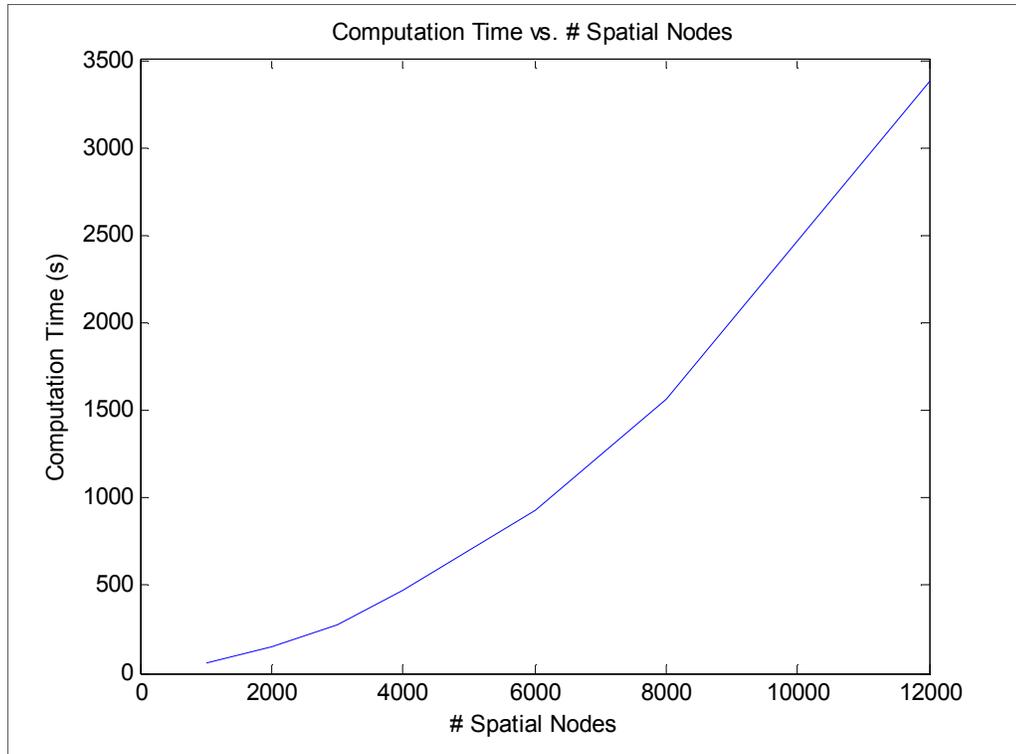
Figure 28: Computation time requirements for a given quantity of spatial nodes

Computation duration results were well within acceptable ranges. With multi-core processors, several test cases can be analyzed almost simultaneously, quickly providing the researcher with large amounts of valid data with which to base their decisions.

5.3   Model Limitations

As shown, the Timoshenko model is quite capable of providing valid beam behavior for a variety of input loads, ranging from static to high speed point loads and rapidly increasing uniform loads. Tests have been conducted using traveling loads which include armature effects created when using "C-shaped" projectiles and these too produce expected beam displacement behavior. However, the damping used within the simulations was approximated based on beam behavior comparisons between the experimental and simulated results. Further experimental data defining the true damping within the system would benefit the software and provide greater accuracy. There arose some issues using damping and the finite difference method in which discontinuities and approximations, particularly at the end locations, which caused the beam to become unstable under excessive damping. This effect can be seen in the convergence plot,

Figure 15, in low spatial node cases. The issue is reduced with the addition of spatial nodes and beam behavior became stable within the simulation time once again.

Additionally, what makes this software faster and more intuitive to use also limits it in some respects. Two dimensional behaviors such as longitudinal displacements which can include Rayleigh surface waves are neglected in the 1-D Timoshenko model.   These are hypothesized to be major contributors to the beam pitting and gouging observed following projectile launches. The additional stress levels generated by these effects below the surface are not accounted for within the model in the form given. It is the approximation of these higher level effects which limit the software.

Chapter 6: Dynamic Load Factor and MATLAB User Interface

6.1   Dynamic Load Factor

A new analysis tool has been used in the understanding of beam stresses throughout a launch. The dynamic load factor (DLF) compares the stresses encountered during a constant acceleration/force or railgun simulation to those encountered during a static loading of the beam using the same force (26).

$$DLF = \frac{\sigma_{dynamic}}{\sigma_{static}} \tag{26}$$

Stresses created during launch due to projectile velocity are more easily assessed using such a tool; a sample plot is shown in Figure 29 for a railgun test fire. The highest calculated bending DLF is plotted against its corresponding projectile velocity value. Bending DLF is a comparison of the maximum bending stresses the rail endures at the surface. In this way, the researcher can quickly and easily interpret the effects of projectile velocity on beam stresses.
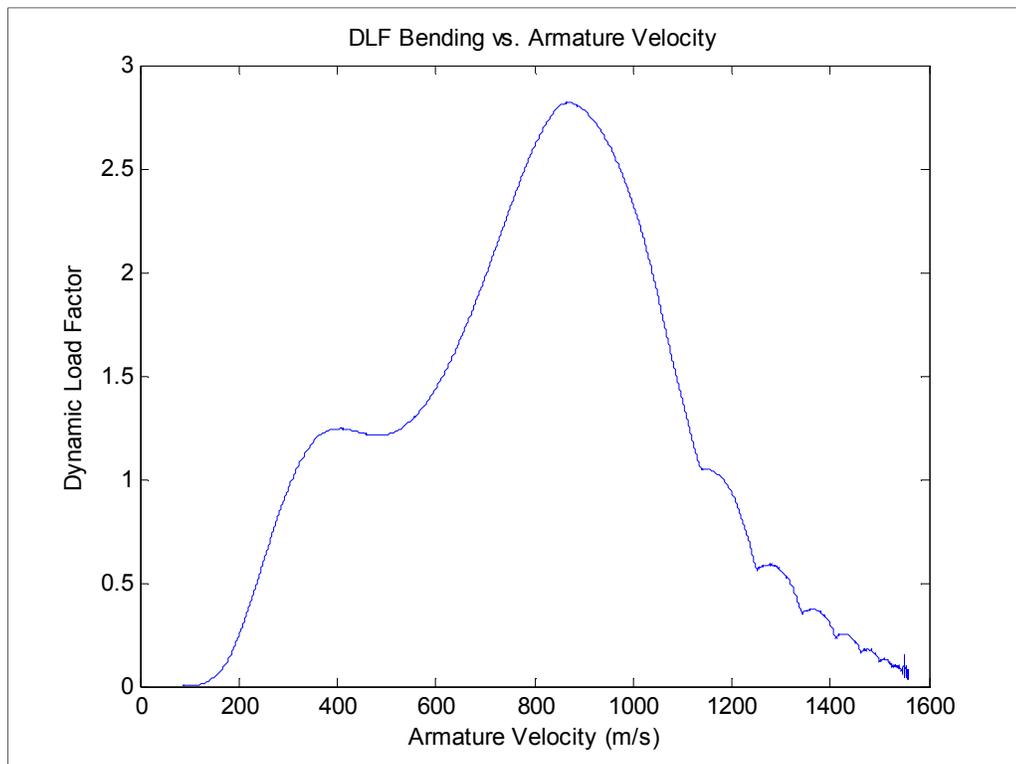

Figure 29: DLF maximum bending stress vs. armature velocity

To calculate the DLF, static load is applied slowly to half of a beam with identical system parameters, oscillations caused by the discretization are allowed to dampen out to a steady state. The peak stress along the static beam is recorded and compared to the peak stress values along the beam for each instantaneous velocity. This ratio is shown on the ordinate as the DLF. As one can see from the plot, a strong correlation exists between the armature speed and the given DLF. Figure 30, Figure 31, and Figure 32 show the other dynamic load factors used: containment shear stress, pressure, and I^2*DLF. The shear stress DLF is indicative of the maximum shear Stresses within the beam, i.e. at the beam neutral axis. The DLF foundation pressure plot measures the force imparted on the beam containment during launch by using the foundation stiffness and the beam displacement.
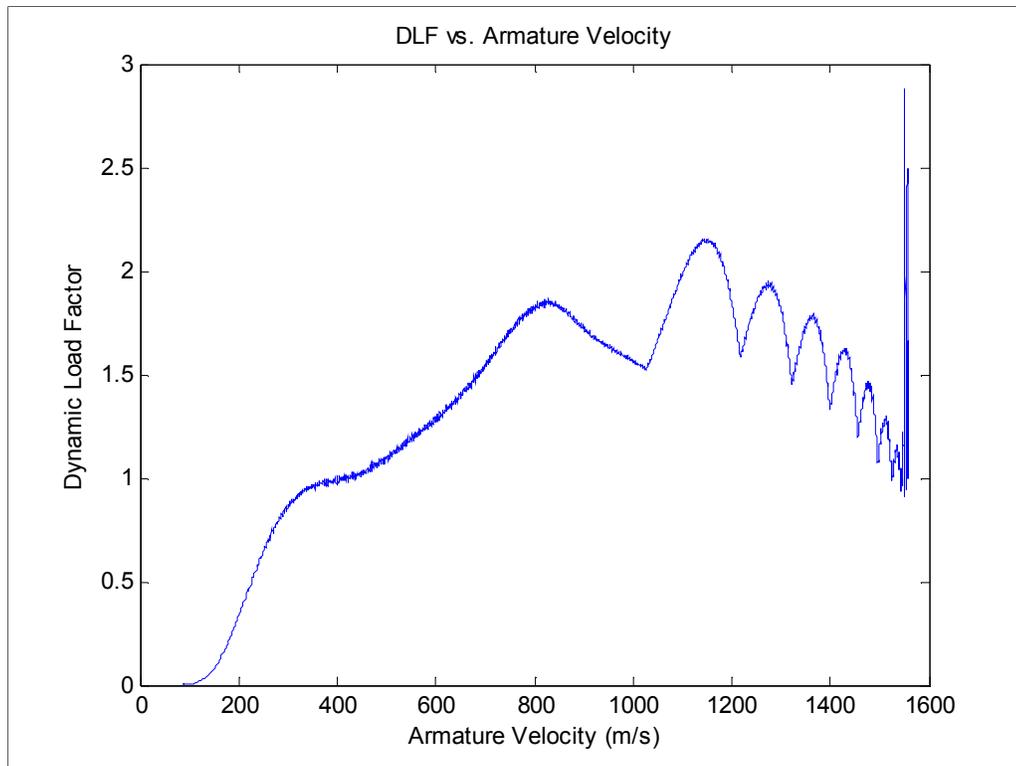
Figure 30: DLF maximum shear vs. armature velocity

Using the assumption that the foundation behaves as a series of linear springs, the force applied is proportional to the beam displacement at any one node. This plot in particular can aid in the design of the containment system used. It is evident from this plot that both the armature speed and wave interaction have a large effect on the deflection of the foundation. Further analysis could yield methods by which the pressure is reduced and the containment life could be extended.
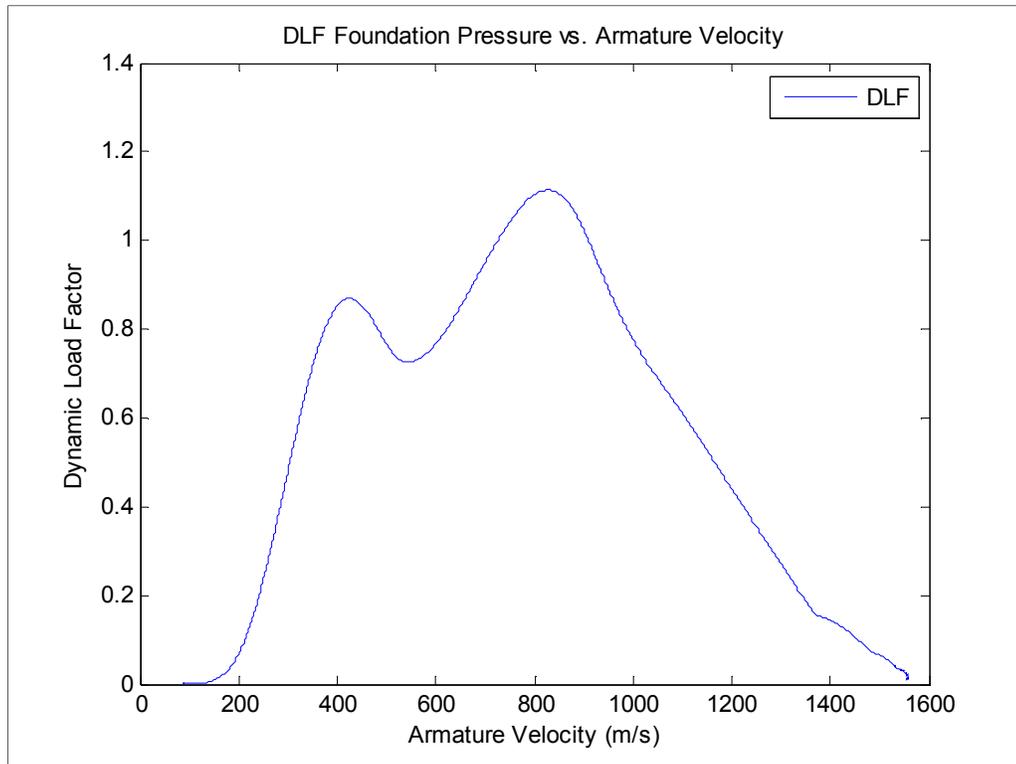
Figure 31: DLF foundation pressure vs. armature velocity

Finally, the I^2*DLF plot is yet another visualization tool similar to the bending DLF however with the I^2 term the DLF has a stronger correlation to the current passing through the beam at a particular velocity value. Though it does not provide any additional insight into the constant current/pressure case, when analyzing a simulated railgun launch, it can help to differentiate the current induced stresses and wave velocity induced stresses. Comparing Figure 29 to Figure 32, one can see for this particular current/position launch profile, the location of the maximum current also coincides with the position the armature is traversing as it passes through the critical velocity. For design purposes, this would be a key element to avoid; suggesting that future systems move these two events to separate beam locations.
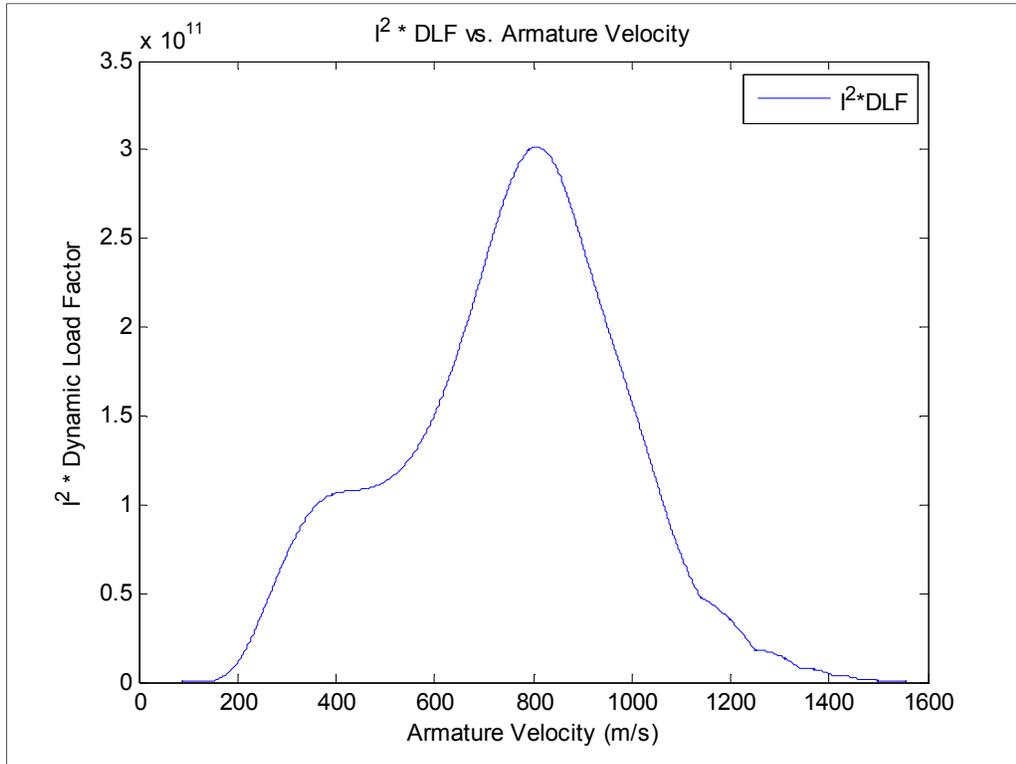
Figure 32: I^2*DLF vs. armature velocity

The DLF calculation is a case specific process and is valid only for the system parameters and peak current outlined in Chapter 3 and Chapter 4. Changing these values requires a new DLF setup allowing for ample settling time when using novel loading values and system parameters.

6.2 Foundation Stiffness Effects

The success of future railgun designs requires the advancement many components, though perhaps one of the most important is the elastic foundation, also known as the containment. This structure, as discussed before, restricts beam motion during projectile launch which in turn has a large impact on the strains and stresses the beam experiences over this time period. Rail material and shape can only go so far in the mitigation of deformation and extension of weapon bore life which raises the need for innovative new designs of the containment structure. The FD approach, coupled with the DLF calculations, provides a series of methods to analyze the effect of varying foundation stiffness for both constant and non-uniform containment designs.

6.2.1 Dynamic Beam Behavior and Foundation Stiffness

As outlined in [11], the foundation stiffness coefficient has a prominent effect on the dynamic response of the beam under load. Beam deflection, thus strain, is reduced for higher

values of foundation stiffness, as shown in Figure 33 for a position 0.05 meters down the rail. This simulation was run using a dynamic characterization input set to 1500 m/s projectile velocity and a railgun-like input magnitude and system parameters. Changing only the foundation stiffness coefficient, the simulation was run using values which corresponded to beam critical speeds of ~821 m/s, ~948 m/s, ~1418 m/s, and ~2171 m/s.
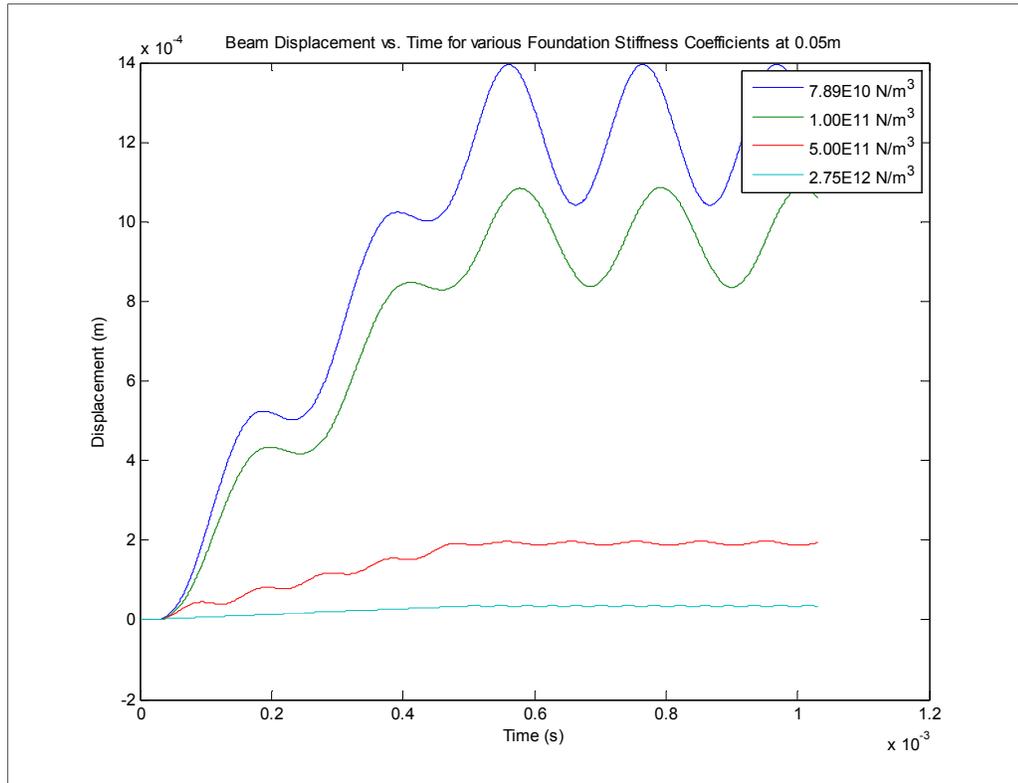
Figure 33: Beam deflection during launch at 0.05m for various stiffness coefficients

As one can see the displacement of the beam is reduced immensely with the use of high foundation stiffness coefficients; maximum displacement of the beam at this location decreasing with the stiffness. Conversely, the frequency of the beam vibration increases, as is evident in both Figure 33 and Figure 34, for the higher stiffness values, which is consistent with traditional mass-spring vibration theory. Limiting the displacement of the beam also limits the bending strains it endures during loading, shown in Figure 34. Increasing the strain over a similar range and analyzing the strain a similar trend is seen though not as sensitive in nature. Where a quintupling of the stiffness coefficient reduced the displacement by similar multiple and slightly increased the beam vibration the opposite is true of the strain. Here the strain amplitude is reduced by approximately 1/3 and the frequency doubled.
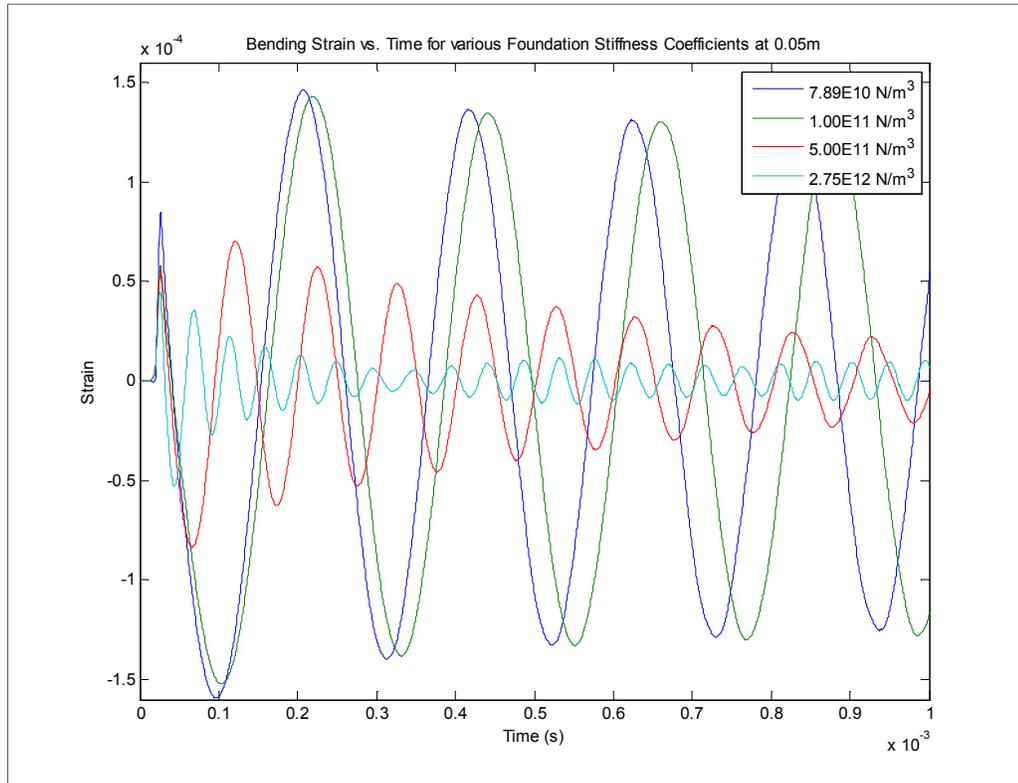
Figure 34: Bending strain during launch at 0.05m for various stiffness coefficients

The analysis of the bending strain would lead a researcher to simply use a large containment structure and maintain a high stiffness coefficient; the use of a uniform foundation is not the optimum or most cost effective solution to the problem, as conventional weaponry has shown for years. The FD Timoshenko model can be applied to systems using variable stiffness coefficients, such as the software spline fit of a plateau/linearly varying setup shown in Figure 35. Basing this test case off of the knowledge that the largest beam strains are experienced during the time of peak current of a weapon launch, the stiffness is held constant at a constant value until this peak has occurred. Both the final and initial coefficients in this case raise the critical velocity, with the initial stiffness being nearly five times larger before linearly decreasing to final stiffness of 1.791×10^{11} N-S/m^2. By using these values, as discussed in Section 6.2.2, the transitional velocity effects are moved farther down the rail.
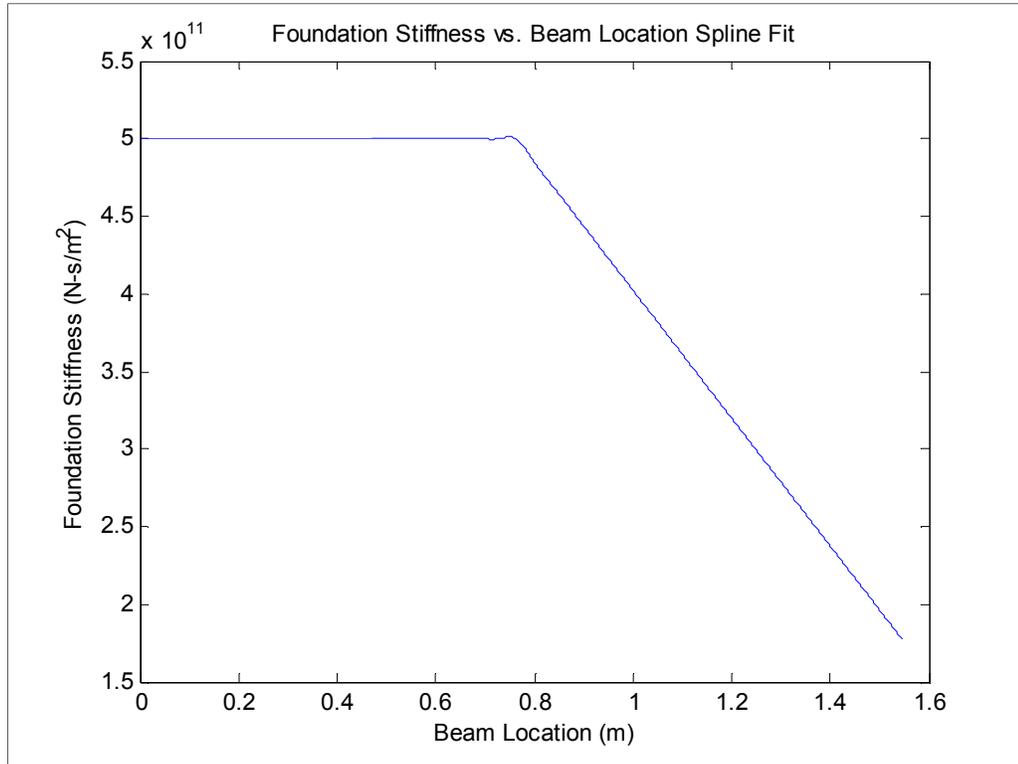
Figure 35: Foundation Coefficient vs. Beam Location

Though only used to show the possible benefits of such systems, this case illustrates that by varying the stiffness to offset the current load and projectile velocity beam stresses and strains can be reduced. Beam strains over the length of the beam become much more uniform in comparison to the constant stiffness simulations in addition to reducing the largest strain by 72%. Greater research into the design of the containment can optimize the balance between containment size, cost, and effect on beam stresses and strains as shown in Figure 36.
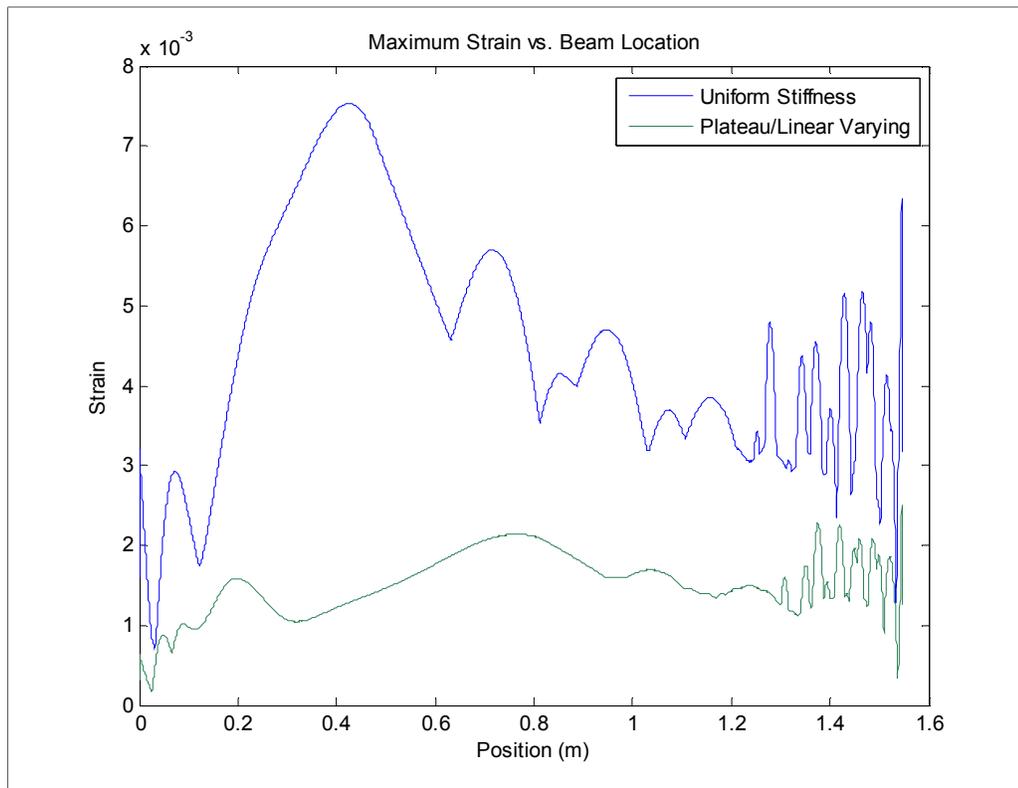
Figure 36: Maximum Strain at each beam location during launch

The need to analyze the compounding effects of velocity and current have been discussed, however with the modification of the foundation stiffness the issues discovered can begin to be alleviated, as discussed using the DLF in Section 6.2.2.

6.2.2 Critical Velocity and DLF

Figure 37 and Figure 38 reflect the impact of changing the foundation stiffness on a given system in order to raise the critical velocity to approximately 1300 m/s. The bending stress has been reduced from a DLF of 3 to 2, indicating the stressed have been reduced by approximately 33%. From Figure 37, two stress peaks are clearly visible at the critical velocity and the velocity during the greatest current draw. The DLF tool identifies crucial moments during the launch of the projectile; using a combination of DLF plots the user can determine the cause of these behaviors.
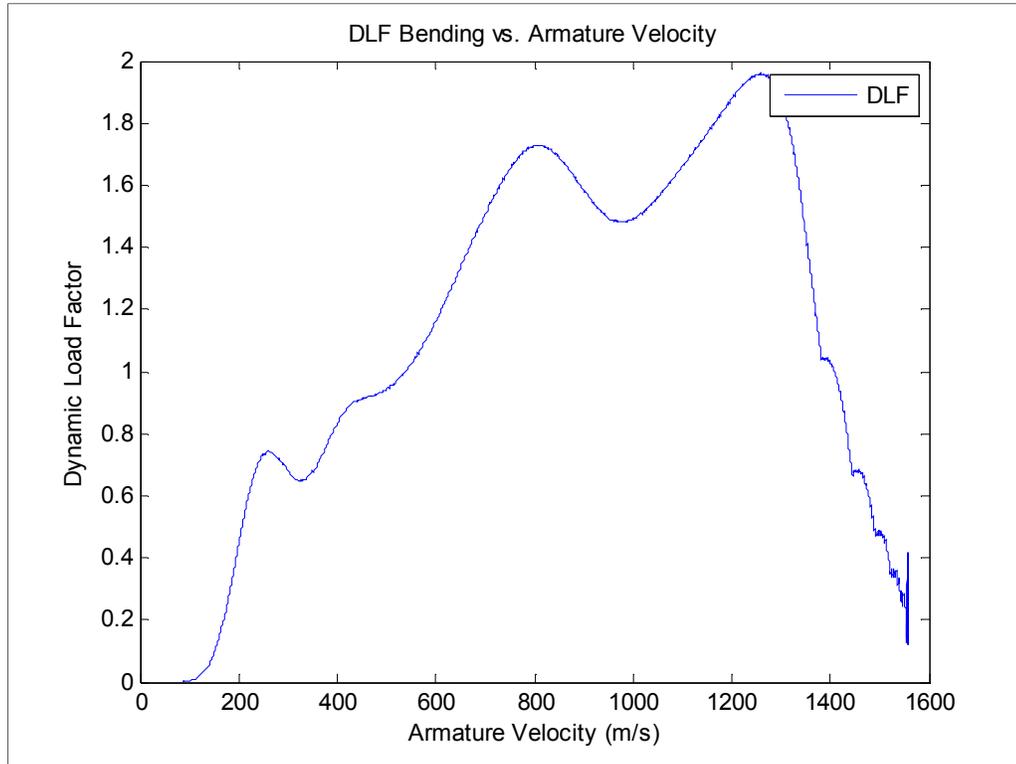
Figure 37: Modified V_{cr} DLF maximum bending vs. armature Velocity

      A comparison between the I^2*DLF plot and the bending DLF plot differentiates the velocity effects from the current effects and allows for a more accurate analysis of beam behavior. Unlike Figure 32 in which the maximum current and critical velocities coincided, Figure 38 is used to locate the highest current and separate it from other effects. When the system parameters dictate that the critical velocity is encountered farther down the rail when the current is reduced, the I^2*DLF plot shows that stresses are reduced by about 1/3.
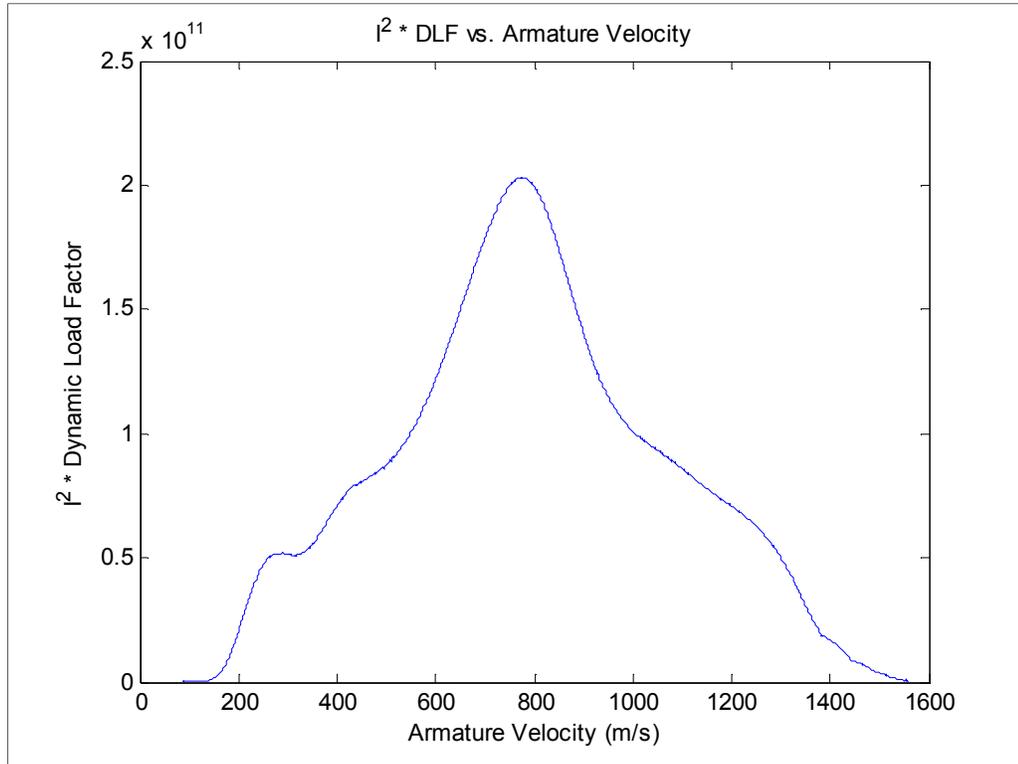
Figure 38: Modified V_{cr} I^2*DLF vs. armature velocity

The DLF tool supports previous research in the field regarding the effect of armature/load velocity and beam stresses and provides a strong development tool for future system designs.

6.3   MATLAB User Interface

In addition producing a working model for accurate prediction of wave propagation a graphical user interface (GUI) was developed for data loading and result analysis. The front panel is simplistic when compared to the earlier mentioned finite element software packages, this is in large part to the reduced complexity of the model and the narrowed range of application. However, it still provides fast and pertinent information for easy analysis of the given railgun or wave analysis simulation. Shown in Figure 39, the GUI consists of four primary components based on the functions they perform, clockwise from the upper-left corner: plot window, input data summary, beam/simulation data input/output, and result analysis tools.
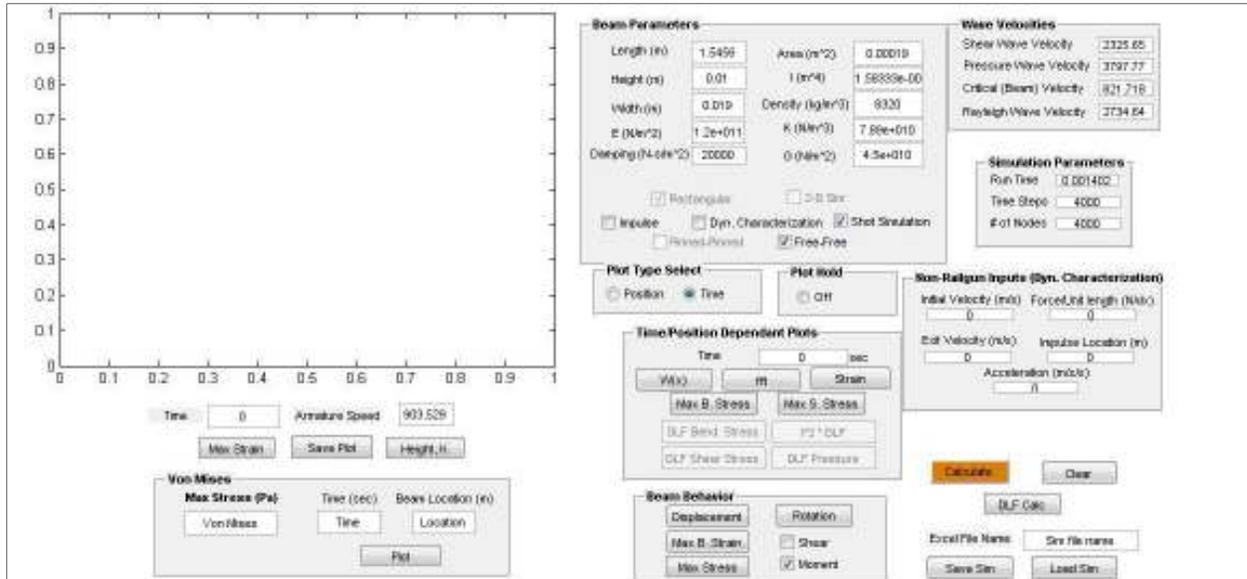
Figure 39: Dynamic rail simulator graphical user interface

The GUI is meant to reduce training time while providing the level of analysis required. The user is able to produce animations of the beam displacement, maximum bending strain, maximum shear or bending stress, or element rotation.   Plots of the beam's displacement, bending strain, maximum shear stress, or maximum bending stress can be produced at the desired time or spatial step. A Fast Fourier Transform (FFT) can be performed on the beam displacement for a given time step to analyze wave length properties. Von Mises stresses can be plotted for a given time and beam location for locations within the beam near the centerline to the surface. DLF plots as discussed in Section 6.2 require additional computation time to determine the static load peak stresses, however each are a simple button press once computation is complete. Maximum bending stress, foundation stiffness, and beam height for each beam location are also plot options for reference. Appendix A outlines the use of each component of the front panel.

Chapter 7: Future Work and Conclusion

7.1   Future Work

Future railgun beam behavior analysis is separated into two components: more accurate experimental data of system parameters/beam behavior and the addition of more complex analysis components both linear and non-linear including two dimensional deflections.

7.1.1 Characterization of System Components

Beam response comparisons between experimental and simulation data were hindered by the capabilities of the detection devices used. Updated strain instrumentation would allow for a more accurate measurement of the Timoshenko model accuracy when compared to experimental data. This becomes especially important as future iterations begin to include ever more complex approximations of non-linear effects such as non-linear foundation response, inelastic beam behavior, armature skipping, and other higher level effects. The ease and intuitiveness of adding such effects became a driving reason to use finite difference approximation for solving the Timoshenko model.

The justification of software additions by way of experimental evidence is required for future iterations; however this can become counterproductive as many such setups can require large financial resources as well. Without accurate experimental data it is impossible to fully understand and correctly model a given railgun setup. Though results may mimic the experimental data, a lack of knowledge pertaining to the given design parameters makes the accuracy of these models pure coincidence; great care was taken in the validation of this software package to use real-world experimental data and ensure a direct relationship between the two. Additional data pertaining to the railgun, particularly state-of-the-art designs, is limited to the public and expensive to obtain, a more cost effective and simplified setup would be highly beneficial.

To aide in the quantification of future rail design parameters, a small scale, low cost, and robust test bed has been developed. This design is approximately 1/3 the size of the current Dahlgren test weapon and uses only a single clamped beam for testing. The design and future testing possibilities are presented in Appendix B. Testing could include wave velocity validation, foundation stiffness matching in conjunction with impulse simulations, and the investigation of novel beam instrumentation prior to use in full scale weapons.

7.1.2 Software Additions

Future software iterations will incorporate a wide variety of additional simulation options, from the addition of various armature shapes to beam modifications. While it was assumed for this paper that the load application was uniform, a more accurate representation would peak pressure loads at the armature location due to the current "C-Shaped" armature. This effect could lead to much higher strains at the onset of the load and new beam behavior. With higher peak loads the design of the entire system would need modification. Along with beam shape one could also add effects similar to those seen in [1], particularly those relating to pressure variation along the length of the armature over the range of projectile velocities. Several methods for implementing these various armature effects have been proposed though implementation has been left for future works.

Current beam design is driven by the electromagnetic effects present when using certain beam shapes and the interaction of the beam with the armature.

7.1.3 Two Dimensional Beam Response

Two dimensional dynamic beam behaviors, as they relate to high speed electromagnetic launchers, have generally been analyzed using complex FE software. As with the one dimensional case, it has been proposed that a simplified model such as the mass-spring-lattice model (MSLM) [12] be used for early analysis. This method can be solved using similar differential approximations and input types used in this thesis.

Two dimensional analyses though computationally more complex, could offer insight into the effects of subsurface rotational motions on railgun bore life and power delivery with the use of small scale simulations. It is well known that these rotational waves do in fact occur, such as those encountered during geological events such as earthquakes, however the impact of this phenomenon during railgun launches is only hypothesized at this time, thus further testing and simulation time is needed.

7.2   Conclusion

The finite difference approach to solving the Timoshenko beam equation with the addition of foundation stiffness, high amplitude forcing function, and damping has been shown to accurately and precisely predict railgun beam response during launch. Based on comparison to experimental data, neglecting effects of armature skipping/arcing, and other complex non-linear effects yet to be added, the model is able to match beam response magnitudes to within approximately 10-20%. The solutions quickly converge to a defined beam shape and displacement magnitude for a relatively low quantity of spatial nodes, thus reducing computation

time and memory requirements. It was shown that for a 1.5456m beam 4000 spatial nodes would sufficiently approximate the beam and its behavior after a computation time of approximately 500 seconds. For greater precision, it was suggested that the quantity be increased to 6000-8000 nodes, though these required significantly more computation time with diminishing levels of return on the resources allocated.   The dynamic load factor analysis (DLF) tool introduces a new method by which to analyze the various causes of beam stress through its launch velocities. Future iterations of this software aim to include more effects, linear or non-linear, to approximate higher level effects seen during experimental launches. The model has been implemented in such a way that the inclusion of such effects would not require large software changes. The exception to this would be the addition of two-dimensional beam behavior for the analysis of Rayleigh surface waves, which would require the implementation of a new model.

References

[1] Johnson, A. J. and F. C. Moon (2006). "Elastic waves and solid armature contact pressure in electromagnetic launchers." Ieee Transactions on Magnetics **42**(3): 422-429.

[2] Frýba, L. (1999). Vibration of solids and structures under moving loads. London, Thomas Telford.

[3] Iglesias, A.M., Wicks, A.L., and Schwartz, T. "Interactions of Modal Analysis and Wave Propagation Using Timoshenko Beam Model"

[4] Schaaf, J. C. and N. F. Audeh (1989). "Electromagnetic Coaxial Railgun." Ieee Transactions on Magnetics **25**(5): 3263-3265.

[5] Bauer, D. P. (1995). "Achieving High-Efficiency with Conventional Railgun Launchers." Ieee Transactions on Magnetics **31**(1): 263-266.

[6] Sun, Y. H., P. Yan, et al. (2009). "Design of a 3-m-Long Electromagnetic Launcher." Ieee Transactions on Magnetics **45**(1): 471-473.

[7] James, T. E. (1997). "Arcing phenomena in transitioned solid armatures." Ieee Transactions on Magnetics **33**(1): 80-85.

[8] Watt, T. and F. Stefani (2005). "Experimental and computational investigation of root-radius melting in C-shaped solid armatures." Ieee Transactions on Magnetics **41**(1): 442-447.

[9] Budynas, R. G., J. K. Nisbett, et al. (2008). Shigley's mechanical engineering design. Boston, McGraw-Hill.

[10] Weaver, W., S. Timoshenko, et al. (1990). Vibration problems in engineering. New York, Wiley.

[11] Liu, W., L. Shi, et al. (2011). "Deformation Calculating of Electromagnetic Launcher's Rail Subjected to Sinusoidal Magnetic Pressure." Mathematical Problems in Engineering:

[12] Yim, H. and Y. Sohn (2000). "Numerical simulation and visualization of elastic waves using mass-spring lattice model." <u>Ieee Transactions on Ultrasonics Ferroelectrics and Frequency Control</u> **47**(3): 549-558.

Appendix A: Software User Guide

Software accessibility and simulation setup time, while secondary to accurate and precise beam modeling, were major design criteria during developing. As stated in previous chapters, the user interacts with the software through an easy to use MATLAB graphical user interface (GUI). All input data is imported through the use of this GUI; time step and node quantity values are directly specified on the front panel, while the remaining information is brought in through excel spread sheets. Below is a step by step procedure for each of the loading options and a general overview of the post-processing plotting capabilities.

Impulse Simulation

1. Specify spatial and temporal node quantities based on rail length and simulation time.
2. Select "Calculate"
3. When prompted, select desired system parameter spreadsheet. Spreadsheet should include (in this order): beam length (m), beam width (mm), Young's Modulus (GPa), Shear Modulus (GPa), beam density (kg/m^3), rail separation (mm), and system damping (N-s/m)
4. Select "Open"
5. When prompted, select desired beam height and foundation stiffness profile. Spreadsheet should include (in this order): beam location (m), beam height (mm), and foundation stiffness (N/m^3)
6. Select "Open"
7. When prompted, select desired load input data. Spreadsheet should include (in this order): simulation run time (ms), impulse location on beam (from left edge) (m), and impulse amplitude (N/m) which can be specified directly or calculated from a desired peak current (A)
8. Simulation calculation time will vary based on node quantity and run length, "Calculate" icon will change in color upon completion

Dynamic Characterization

1. Specify spatial and temporal node quantities based on rail length and simulation time.
2. Select "Calculate"
3. When prompted, select desired system parameter spreadsheet. Spreadsheet should include (in this order): beam length (m), beam width (mm), Young's Modulus (GPa), Shear Modulus (GPa), beam density (kg/m^3), rail separation (mm), and system damping (N-s/m)
4. Select "Open"

5. When prompted, select desired beam height and foundation stiffness profile. Spreadsheet should include (in this order): beam location (m), beam height (mm), and foundation stiffness (N/m^3)
6. Select "Open"
7. When prompted, select desired load input data. Spreadsheet should include (in this order): initial velocity (m/s), final (exit) velocity (m/s) and constant current load (A)
8. Simulation calculation time will vary based on node quantity and velocity values, "Calculate" icon will change in color upon completion

Railgun Shot Simulation

1. Specify spatial and temporal node quantities based on rail length and simulation time.
2. Select "Calculate"
3. When prompted, select desired system parameter spreadsheet. Spreadsheet should include (in this order): beam length (m), beam width (mm), Young's Modulus (GPa), Shear Modulus (GPa), beam density (kg/m^3), rail separation (mm), and system damping (N-s/m)
4. Select "Open"
5. When prompted, select desired beam height and foundation stiffness profile. Spreadsheet should include (in this order): beam location (m), beam height (mm), and foundation stiffness (N/m^3)
6. Select "Open"
7. When prompted, select desired load input data. Spreadsheet should include (in this order): time location (ms), armature (load) location (m), and current (A). NOTE: Actual values used in software are spline fit approximation of these curves, greater detail in spreadsheet will create more accurate simulations though is not required
8. Simulation calculation time will vary based on node quantity and shot time, "Calculate" icon will change in color upon completion

Dynamic Load Factor Calculation

Though not an actual loading option, but rather a modified version of the dynamic characterization simulation, this simulation is initiated after a dynamic characterization or railgun shot simulation has already been run and is in memory; the "DLF Calc" pushbutton remains inactive until this is completed.

1. Select "DLF Calc"
2. When prompted, select desired load input data. Spreadsheet should include (in this order): time location (ms), armature (load) location (m), and current (A).

3. Simulation calculation time will vary based on node quantity and shot time, "DLF Calc" icon will change in color upon completion

   NOTE: DLF calculation is design case specific and at the time of this thesis is valid only for the system parameters and peak current outlined in Chapter 3 and Chapter 4. Changing these values would require a new DLF calculation spreadsheet.

Post-Processing Capabilities

These tools are used to analyze the displacement, stress, and strain of the beam during the loading event. Static plots, representing the behavior of a single beam node or the behavior of the entire beam at a particular time step, are well suited for quantitative analyses. The beam behavior plots, in contrast, are better suited for a qualitative of beam behavior as these are animations meant to show rail response during loading. Finally, the Von Mises stress analysis tool plots the plane stresses within the beam by approximating the shear and bending stresses using the moments and shear forces experienced at each node.

Time/Position Dependant Plots

Figure 40shows the controls for the time/position static plots. The user first selects the plot type, either position or time, which indicates which type of location (spatial or temporal) he/she will indicate. Once the time or location is entered in the appropriate field the user simply uses the array of push buttons to analyze the various beam attributes when loaded. Data plots can be "held on" for comparison to similar plots by toggling the "Plot Hold" switch.
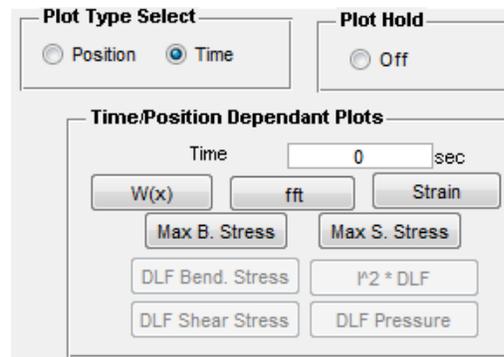

Figure 40: Static position/time dependant plot controls

Dynamic Load Factor Plots

The use of dynamic load factor plots requires additional calculation time after the initial load simulation has been completed; the push buttons remain inactive until this time. Time and location inputs do not impact results, selecting one of the four options plots the given DLF against armature velocity.

Beam Behavior Animations

Dynamic beam response, strain, stress, and nodal rotation are animated using the beam behavior options shown in Figure 41. Displacement, maximum bending strain, and rotation animations are displayed simply by selecting the appropriate pushbutton. Maximum stress animations are viewed by first indicating which type of stress is desired, shear or bending, and then selecting the push button.
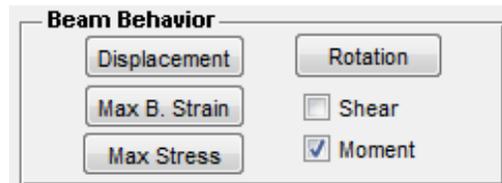
Figure 41: Beam behavior animation controls

Von Mises Stress Analysis

Finally, the plane stresses at locations within the beam, are analyzed using the Von Mises stress analysis tool. The interface for the Von Mises tool is shown in Figure 42. The user specifies the time and beam location to be plotted and selects "Plot." The Von Mises stress is plotted against distance above the beam's neutral axis and the max stress experienced is shown in the GUI window.
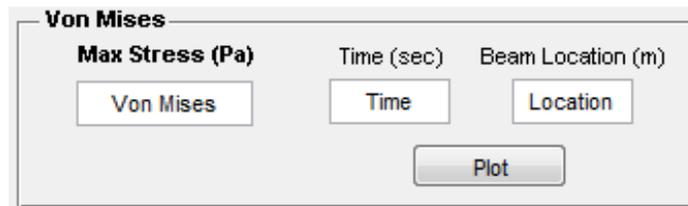
Figure 42: Von Mises stress analysis interface

Appendix B: Scale Test Stand Design

This appendix will outline the design and justification of a scaled test bed for the analysis of wave propagation through a metallic railgun rail. The design consists of an approximately 1:3 scale model of a full railgun. This leads to a test bed with a 50.4mm x 50.4mm x 3048mm metallic rail, which is clamped by G10 material for 2748mm, leaving a section of the rail exposed as a cantilever beam, shown in Figure 43. Clamping force is provided by 60 bolts even spaced along the G10 blocks. The rail is supported by two interchangeable insulation blocks; these blocks provide a method by which to change the stiffness of the system to match the characteristics of the full scale rail.
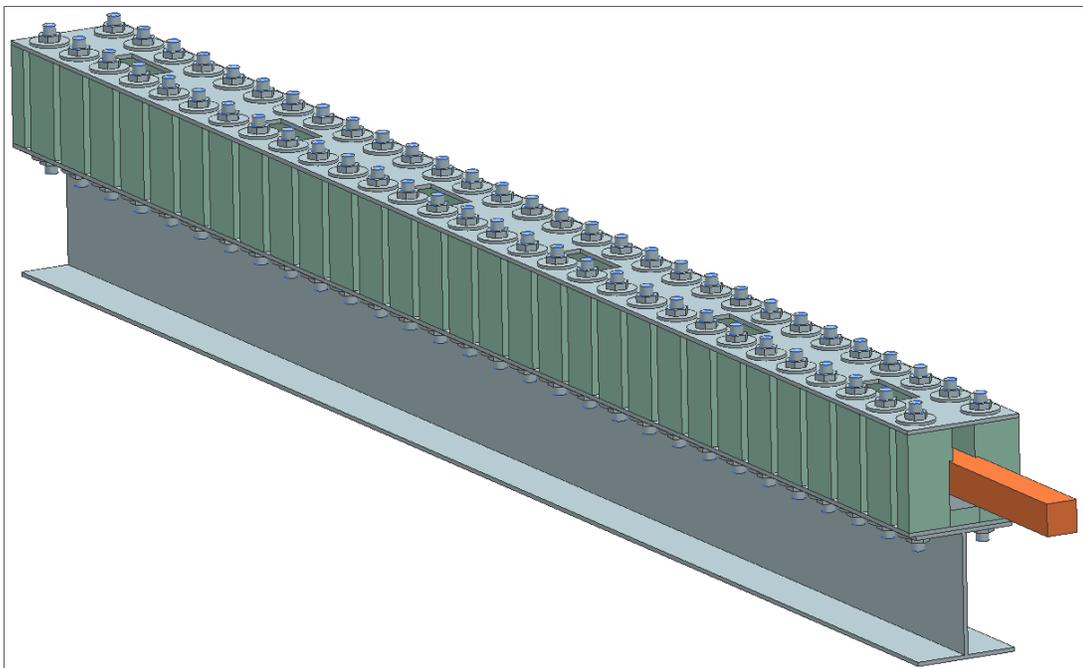

Figure 43: 1:3 scale Rail Test bed

A brief discussion of the system design requirements for the rail test bed are given, followed by the proposed design and a more detailed test bed description along with the finite element analysis. Next will follow suggestions for clamping pressure sensing methods as well as stud torque measurements in order to validate the FEA models and ensure uniform clamping along the entire length of the rail. Finally a summation of test bed components and bill of materials will be presented.

Test Bed Requirements

Design of the railgun test bed was proposed by the NSWC/Railgun Lab, as such, several design requirements were given for size and operation. The following section will discuss in detail the need for a similarly proportioned, easily configurable, and conveniently instrumented testing setup.

Size Specifications

The proposed size specifications for the rail test bed were to be for a rail approximately 1:3 scale of the fully operational device. This leads to a test bed with a 50.4mm x 50.4mm x 3048mm metallic rail, which is clamped by G10 material for 2748mm, leaving a 300mm section of the rail exposed as a cantilever beam for load application and gun breach simulation, as shown in Figure 44.
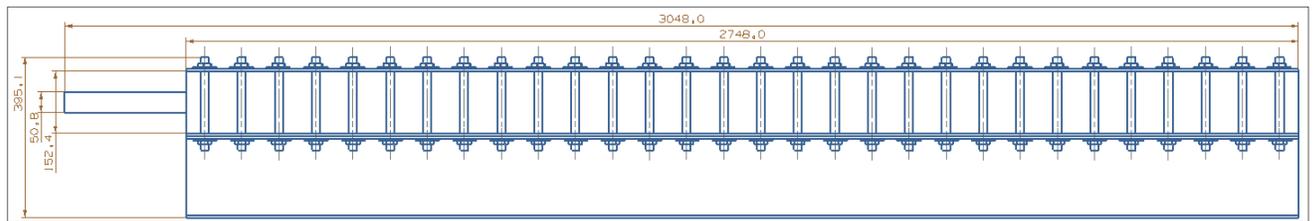

Figure 44: Overall test bed size, dimensions are in mm

Clamping is provided by the G-10 material loaded at 60 points by threaded studs. Further specifications and system parameters will be discussed in the "Test Bed Assembly Design."

Configurability

Analysis of rail characteristics was to be modeled for various elastic supports and rail clamping forces, thus a test bed in which the researcher can only analyze a small range of system parameters without significant effort to modify them is unacceptable. The design must allow for setup modifications without excessive downtime, along with this it must be simple and robust enough to be modified frequently while still retaining its structural integrity. The solution to this design challenge is discussed in the "Test Bed Assembly Design" section of this lab specifically the "Elastic Base" and "Clamping" sub sections.

Ease of Instrumentation

Complete understanding of wave propagation through the rail requires measurements of its reaction at various locations over its length. This not only included locations along its top surface but on all four longitudinal sides. The test bed is to be used for validation of future sensor technology, such as Fabry-Perot or Fiber Bragg Grading optic sensors. These sensors will require implementation at a variety of locations on the beam, thus each location (face) must have

access and wire routes. Further discussion of the implementation of these access points is given in the "Instrumentation Considerations" section of this report.

Test Bed Assembly Design

Overall Design

The design of the test bed is intentionally simplistic, over complication would likely reduce the repeatability of testing and ease of use/configurability. As discussed in the introduction, the stand uses 60 threaded studs to apply a clamping force to a block of insulation material which in turn clamps a metallic rail, as shown in Figure 45.
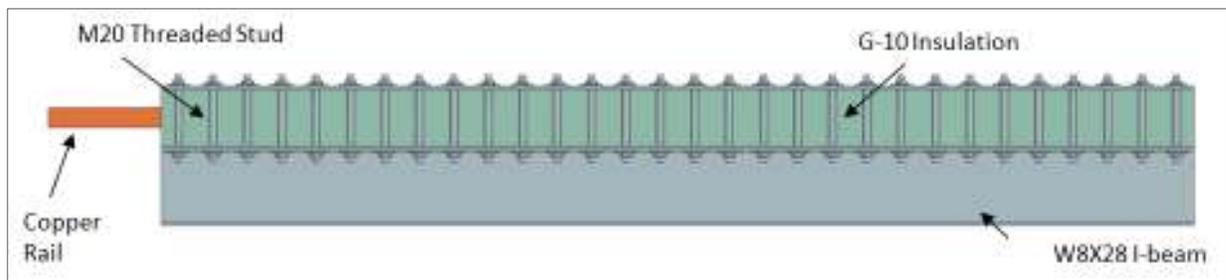

Figure 45: Shaded side view of test bed illustrating stud placement and design component placement.

The whole test stand is supported by a W8x28 wide flange I-beam anchored in place to its surroundings so as to prevent movement, at the time of this report writing the anchoring method was undetermined. A 6.35mm thick steel plate rests on the I-beam for the purpose of supporting the entire width of the G-10 insulating material, some load dispersion, and assisting in the alignment of the threaded studs. As requested, 50.8mm of elastic base material which consists of two interchangeable beams are compressed between the rail and the steel base plate. On either side of the rail is 152.4mm of G-10 insulation, as shown in Figure 46, which can be replaced by any elastic solid, should the design setup deem it necessary. Of the 152.4mm, there is an even distribution of material above, below, and to the side of the rail.
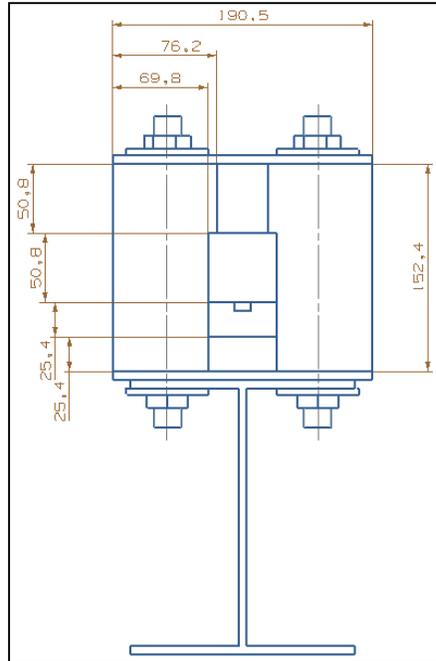
Figure 46: G-10 insulation material dimensioning

This was done upon discussion with the project leaders so as to remain proportional to the full-scale railgun. Above the G-10 material is another 6.35mm steel plate which, along with the bottom plate and I-beam holes, serves to align the studs. This plate has 6 rectangular slots cut along its length to provide the researcher with access to sensors at various locations on the rail, as shown in Figure 47. The steel top plate and flat flange of the I-beam ensure that the bolts remain vertical and clamping force is applied directly down to the G-10/rail and not at an angle which should shift the rail or create additional lateral stresses in the G-10 or rail. The key features of this design are related to changing the system parameters for rail response testing.
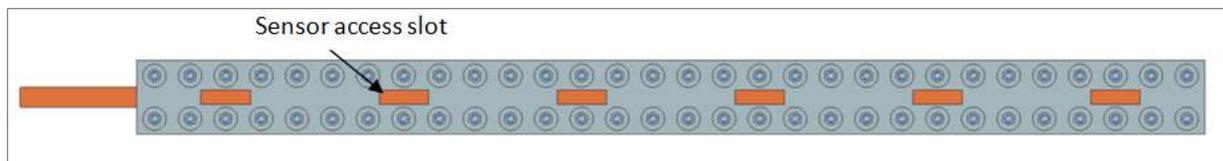

Figure 47: Shaded top view of design illustrating sensor access slots

Elastic Base

As stated in previous sections, the design incorporates removable support beams as labeled in Figure 48. These two beams are shown in the figure as being steel and the G-10 material used throughout the test bed.
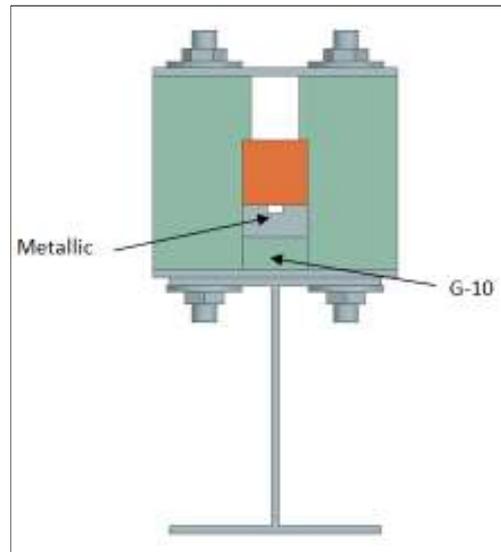

Figure 48: Shaded end-view of design illustrating the removable support beams

Ideally, however, the researcher conducting the experiment would have access to multiple beam materials and thicknesses in order to mimic the full-scale system setup being analyzed. In addition to various support materials, it is also possible to change the material above or to the side of the rail. The G-10 material used mirrors the current elastic foundation material used in the Dahlgren labs; the fiber resin could be exchanged for a stiffer or softer material depending on the requirements of the user.

Clamping

The clamping of the rail is accomplished through a combination of 60, M20 threaded studs and the accompanying washers and nuts torqued in order to impart a pressure upon the G10, shown in Figure 49. These studs were spaced to apply even clamping pressure to the rail along its length as derived from the analysis discussed in the "Clamping Stud Spacing" section of this document.
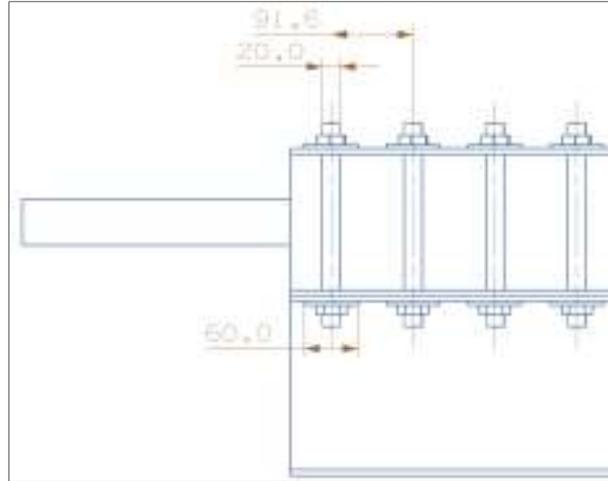
Figure 49: Side sketch of test bed showing clamping components and spacing

The desired pressure to be placed on the rail is a parameter to be varied in the analysis, and so, the design incorporates easy modification of this force by adjusting the stud preload. Measuring the torque on each stud is discussed in the "FEA Validation" section of this report, the torque at each application point must be as close the nominal value in order to provide adequate uniform pressure upon the rail and support the results obtained from the finite element analyses conducted.

Instrumentation Considerations

Sensors are to be placed at a variety of locations along the length of the rail, covering all longitudinal sides. These sensors must be as accessible as the system allows and because they are wired, must have pathways for the various wires that power and transmit data to/from them. The bottom face of the rail rests on a support beam, in which, has been machined a groove for sensor placement. Though the grove is shown centered, because it is interchangeable, it can be offset in order to take measurements from different locations along the width of the rail. The top face of the rail is open and is easily accessed through the rectangular slots shown Figure 48, thus the instrumentation can be change on the top face without deconstruction of the rail. Replacement of the side or bottom sensors requires the loosening of the clamping structure and removal of the beam. The sensor locations on the side faces of the rail will be determined at a later date.

The various design components discussed have been incorporated into the final test bed design, shown in an isometric view in Figure 50. The success of the design depends on its ability to withstand a large range of loads and transfer those loads onto the rail evenly for accurate representation of the full-scale system. This success is discussed in the "Finite Element Analysis" section of this report.
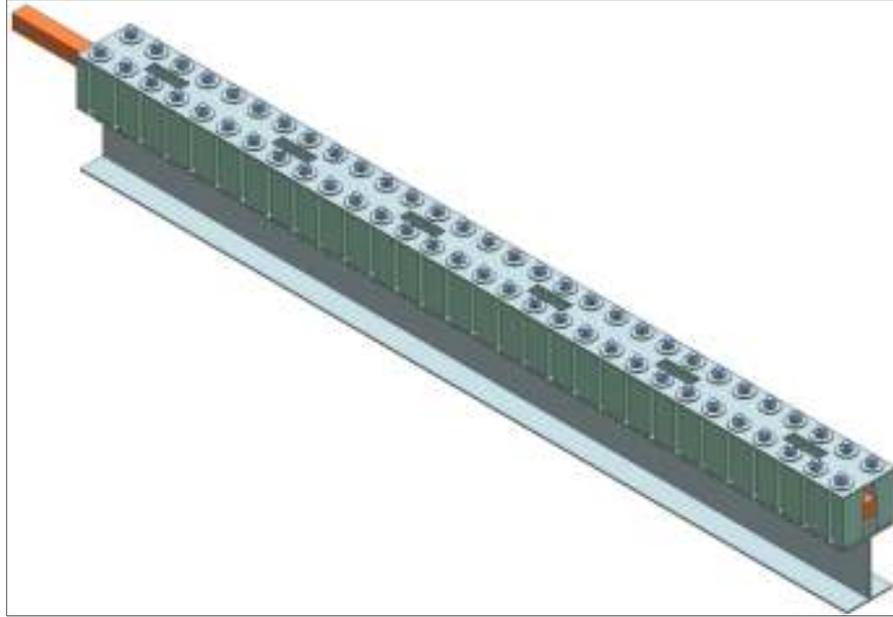
Figure 50: Overall isometric view of final design

Finite Element Analysis

Much of the system design depended upon the capabilities of the G-10 material to withstand and distribute the pressures applied by the clamping studs. As discussed in previous sections, an even load must be applied along the entire length of the rail in order to accurately simulate the wave propagations during testing. This report section will outline the design steps and analysis used to ensure these requirements were met, including the considerations given to clamping stud spacing, G-10 shearing, and loading of the metallic retaining top plate.

Finite Element Setup

The finite element analyses were completed on a simplified geometry consisting of two blocks of G-10 material, a shortened section of the steel top plate, and very thin extrusions from the steel surface at each stud hole, simulating the areas acted upon by the washers. Figure 51, shows this setup for the proposed design.
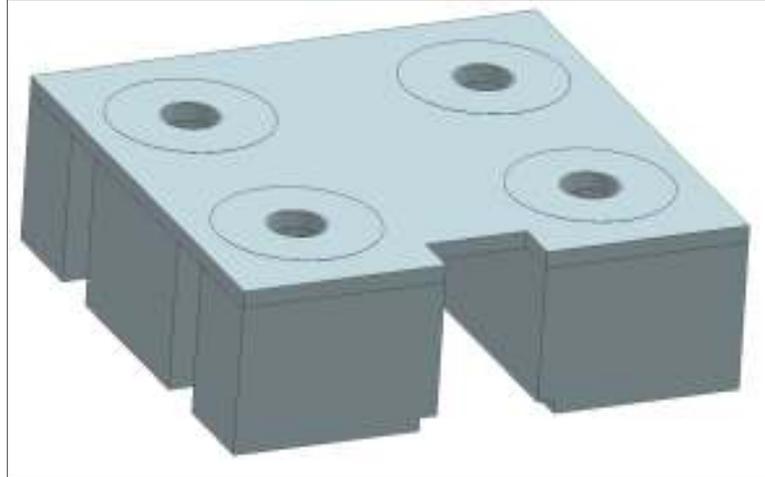
Figure 51: FEA simplified part geometry

The two bottom blocks use the G-10 material properties provided by the naval research group at Dahlgren, specifying a modulus of elasticity of 10 GPa and a Poission ratio of 0.234. Along with the shear strength provided by the manufacturer of 131 MPa the G-10 material adequately defined for the model. The steel plate was approximated using the pre-loaded NX6 properties for steel.

Figure 52, shows the loading and constraints placed on the model for analysis. Four pressure locations are in the model, one for each of the 4 washers present, each loaded at 4000 psi (27.58MPa). The G-10 was fixed at its base which would be its contact point with the bottom steel plate; this approximation was needed to adequately constrain the model for computation. The second set of constraints were applied to the rail contact surface, unlike the fixed constraint in which the nodes have no degrees of freedom, these were setup to be simply supported surfaces. This allows for rotation in all directions, and translation in every direction but the support direction, i.e. the G-10 is simply resting on the rail as it would in the real test bed. The final constraint imparted on the model was the surface "gluing" of the G-10 to the steel, while some slipping may occur in the real design should large displacements occur, these were assumed negligible and the surfaces remain fixed.
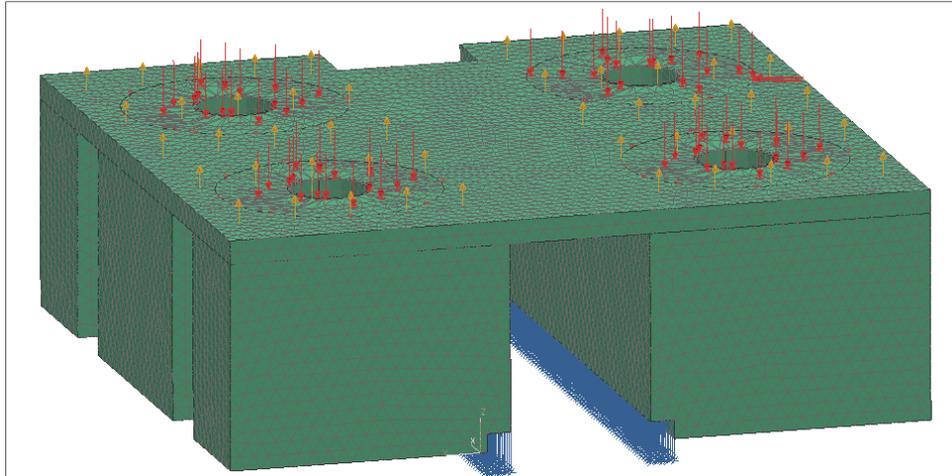
Figure 52: FEA loading and constraints

As shown in Figure 52, the simplified geometry has been meshed. This meshing is a compromise between system memory and computing power and the resolution of the analysis. The G-10 materials, which was the focal point of the analysis was meshed using CTETRA(10) which produces mid-side nodes on a 4 sided figure with element size of 4mm. The plate was modeled using 4mm elements as well however it used the less complex CTETRA(4) for its element definition. Though only moderately resolved, this compromise still yielded acceptable results, as discussed in the following sections.

Clamping Stud Spacing

The primary function of the G-10 material in the assembly is to apply clamping to the G-10, unlike the fully operational railgun the material is not being used for its dielectric and flame retardant capabilities, but instead to mimic the structural base properties. The clamping force applied by this material, as previously stated, must be equal over the length of the rail which is accomplished by the appropriate spacing of the clamping studs in conjunction with washers and the steel retaining top plate. The washer and plate serve to disperse the applied load over a slightly greater G-10 surface area and avoid local surface crushing of the G-10 material. The plate also stabilizes the G-10 vertically and provides a surface perpendicular to the G-10 on which to apply the clamping forces from the washers. The use of the steel plate also serves to ensure consistent assembly of the test bed. The plate has predrilled holes at 91.6mm intervals starting 45.8mm from the plate edge and is 40mm from the G-10 sides, as shown in Figure 53.
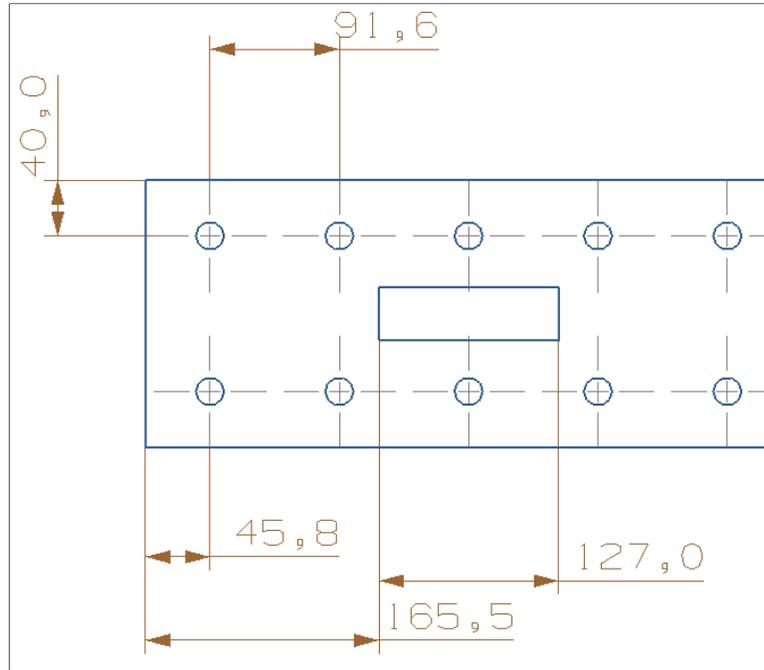
Figure 53: Sketch of top retaining plate showing hole spacing

The 91.6mm spacing was developed from a combination of hand calculation approximations and finite element analysis in NX6. The hand calculations used were simplistic extensions of the pressure cone method in Shigley's Mechanical Engineering Design [8], in which one assumes that the pressure extends through the material at a given angle, α, of $30°$ from the area of contact, which are the 30mm O.D. nuts in this case. Uniform pressure at a depth of 2in. (50.8mm) from the top surface of the G-10 material is was required, as this is the location of the beam/containment interface. The calculations did not include the 0.25 in. plate and washers in an effort to obtain a conservative bolt spacing, which was calculated to be 108.66mm from bolt center to bolt center, starting 108.66mm from the edge. Figure 54 shows this spacing after including 50mm diameter washers.
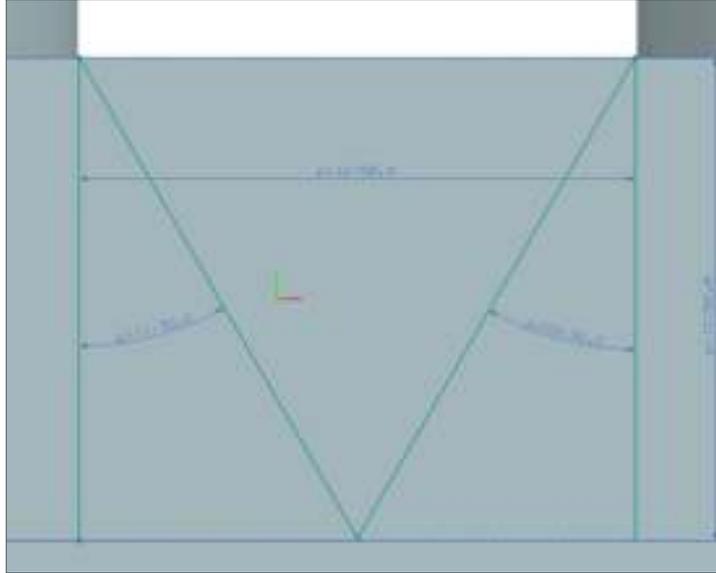
Figure 54: Bolted join pressure cone approximation using 30° cone angle

This spacing implies that approximately 25.29 bolts be used on each side, in order to ensure adequate distribution, this was rounded to 26 bolts per side and so 52 bolts total, with a spacing of 101.78mm. The end bolts were spaced at half the previous interval with minimal loss of contact pressure over the end of the G-10.

Finite element analysis (FEA) of this assembly, however, did not fully agree with this result as is shown in Figure 55. One can see, the reaction forces upon the G-10 are not on the same order of magnitude and vary as much as 82% from an approximated nominal pressure of 36.4N.
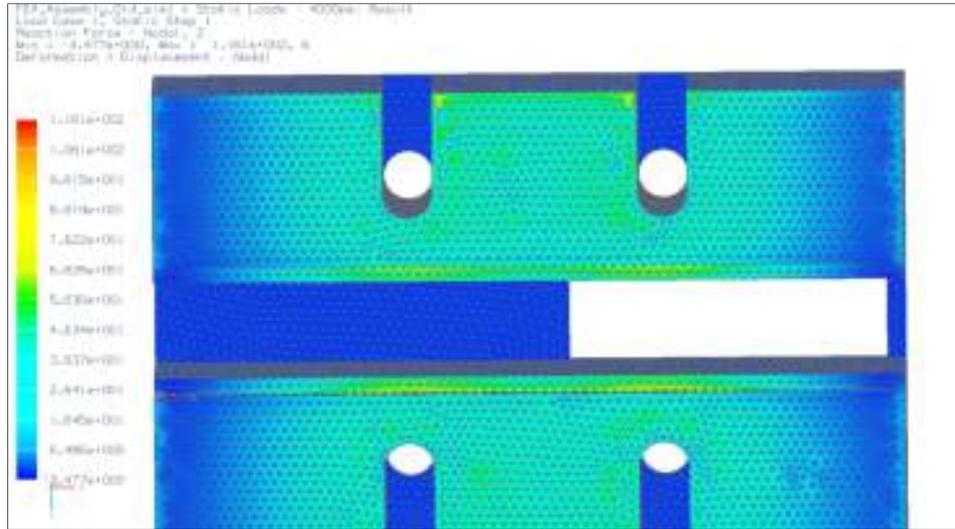
Figure 55: FEA of reaction forces on rail for bolt spacing of 101.7

The gradient shows that the reaction forces are greatest in a radial pattern centered on the bolted joints, as was predicted by the pressure cone approximation method. Upon examination of the finite element results, and after several iterations, it was discovered that the pressure distributes at an angle less than the 30^0 predicted by Shigley's[8], thus requiring shorter spacing and a greater number of clamping studs. The updated design incorporated the 60mm washers shown in the "Test Bed Assembly" section of this report and the steel retaining plate. With these additions into the analysis the distance between studs should have been increased, however, the FEA analysis once again indicated that tighter bolt spacing was needed. After several iterations, it was found that the use of 30 studs per side yielded good pressure distribution across the rail, as shown in Figure 56. The 30 stud design placed the spacing at 91.6mm for interior studs and moved the ends to 45.8mm from the material edge. The denser spacing reduced the pressure variation to 15% along the centerline of the rail surface; this was based on an approximate nominal value of 60N.
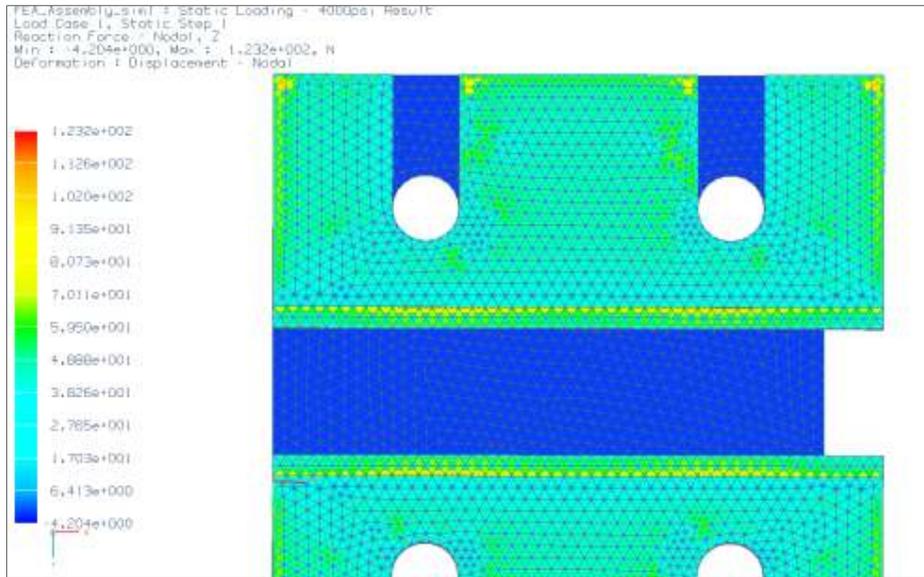
Figure 56: FEA of reaction forces on rail for bolt spacing of 91.6mm

The slightly larger variation transverse to the rail is a by-product of the radial dispersion of the pressure through the G-10, this cannot be avoided. Sixty bolts provided an adequate balance between the practicality, i.e. setup and modification time, and cost of using a large quantity of bolts against the need for minimal pressure variation.

Qualitatively, the changes are clearly visible in the gradient shown along the rail, the color distribution representing the force distribution is much more uniform, though forces peak and valley at finite element nodes, the surface viewed as a whole is quite uniform. These distributions are developed from an analysis which is limited in resolution by the computational and data storage capabilities of the computers used in their generation. With the approximations and partially limited resolution of the finite element models it was decided that the pressure distribution produced by a spacing of 91.6mm is acceptable and shall be evaluated by pressure sensing methods in the constructed model.

Top Plate Distortion

A finite element analysis was also completed to determine if the 6.35mm steel top plate would undergo any significant bending as a result of the compressive loads along its edges. Figure 58 shows the resulting displacement of the plate and G-10 materials as a result of the loading. As one can see from the scale on the left of the figure, for the 4000 psi loading upon each of the washers, the maximum displacement in the negative z-direction, shown as a downward displacement in the figure, of the plate's center is approximately 0.04mm. The maximum displacement occurs at the location of maximum stress, Figure 58 shows this displacement value while Figure 59 shows the calculated Von-Mises stresses which cause this

displacement, this figure is discussed in greater detail in the "G-10 Shearing/Compressive Strength Analysis" section of this report.
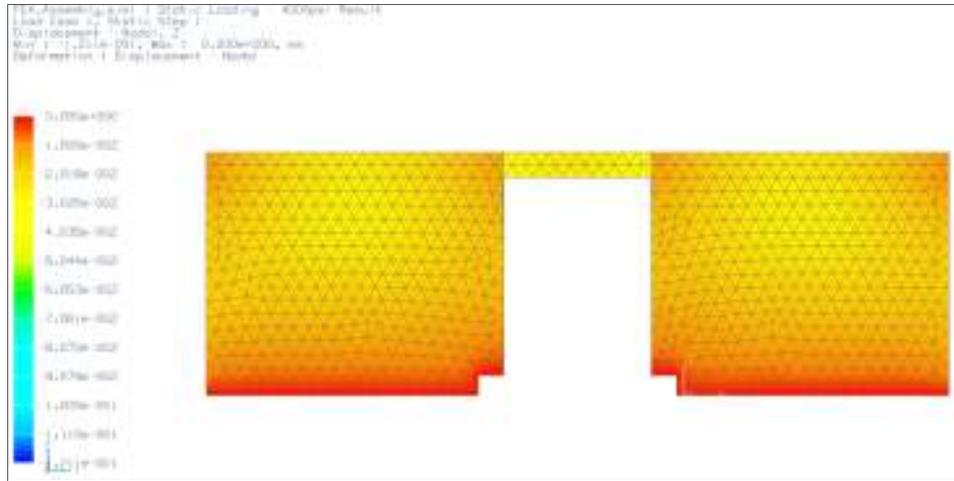

Figure 57: Retaining plate and G10 displacement for 4000 psi washer load

The greatest displacement occurs at the stress concentration areas caused by the circular stud cutout locations and in the unsupported steel plate which crosses the cutout section. These displacements are still on the order of 0.1mm, and represent the distortion caused by a loading that is nearly at the limit the G-10 can withstand in compression, which is covered in the "G-10 Shearing/Compressive Strength Analysis" section.
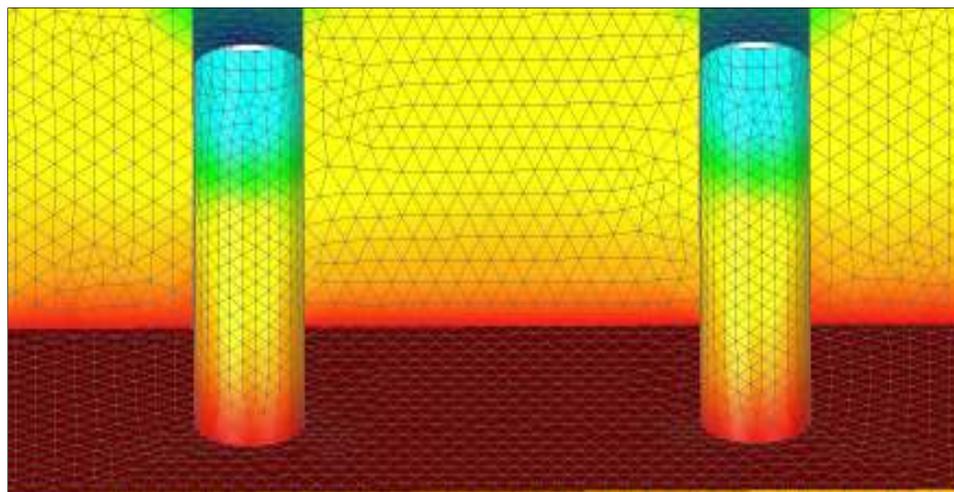

Figure 58: Maximum retaining plate and G10 displacement for 4000 psi washer load

The steel top plate also experiences the greatest stresses in the model, about 289 Mpa, however this is well below its compressive yield strength of approximately 2000 Mpa. From this analysis, it can be seen that the distortion of the top steel plate is not a driving component of the test bed design, which leads to the analysis of the proposed insulation material, G-10, which will be shown is a much greater limiter of the applied loads than the steel plate.
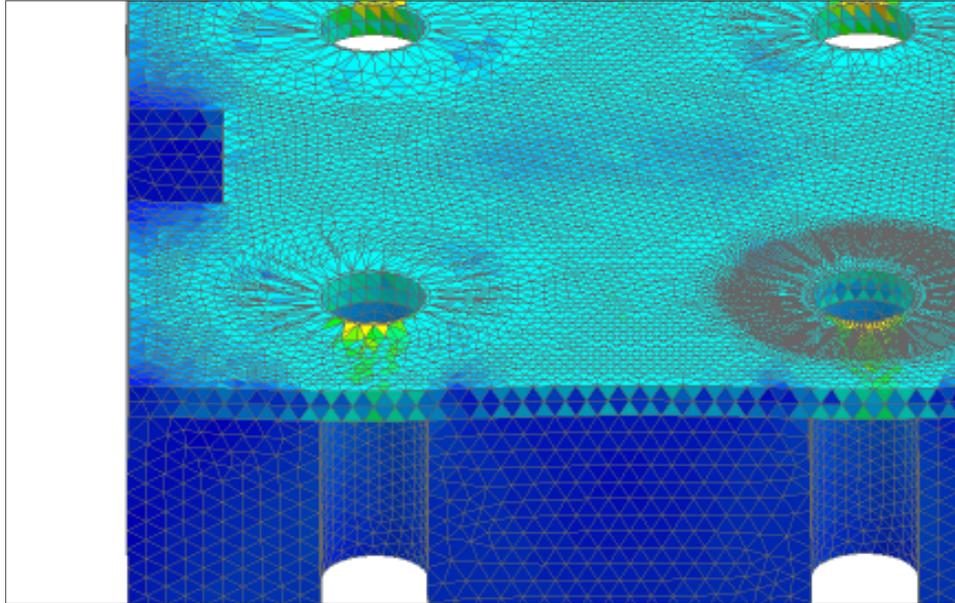

Figure 59: Maximum Von-Mises stresses in model

G-10 Shearing/Compressive Strength Analysis

The design of the test bed was partially driven by the shear stresses imparted into the G-10 material by the clamping studs, especially at the notch location where the rail is loaded, shown in Figure 60. The manufacturer lists the shear strength of the G-10 material as 19,000psi (131MPa) thus the stress within the material should not approach this value.
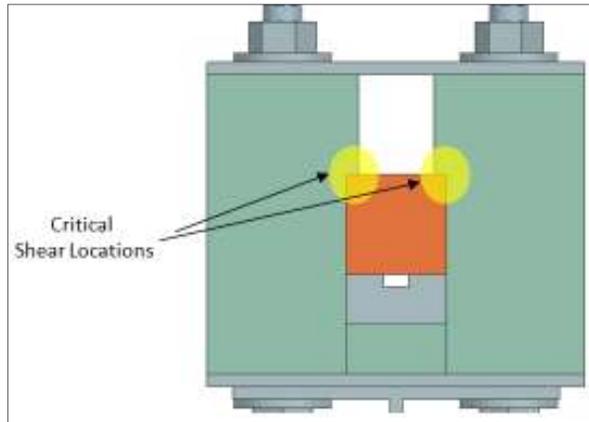
Figure 60: Critical shear stress locations

From the same finite element analysis as discussed in the previous sections, a stress analysis was complete. The resulting Von-Mises stresses from the analysis are shown in Figure 61. The maximum shear stresses in the notch, as was previously thought to be the critical location, were found to be on the order of 50-70 Mpa, which is well below the manufacturer's stated shear strength.
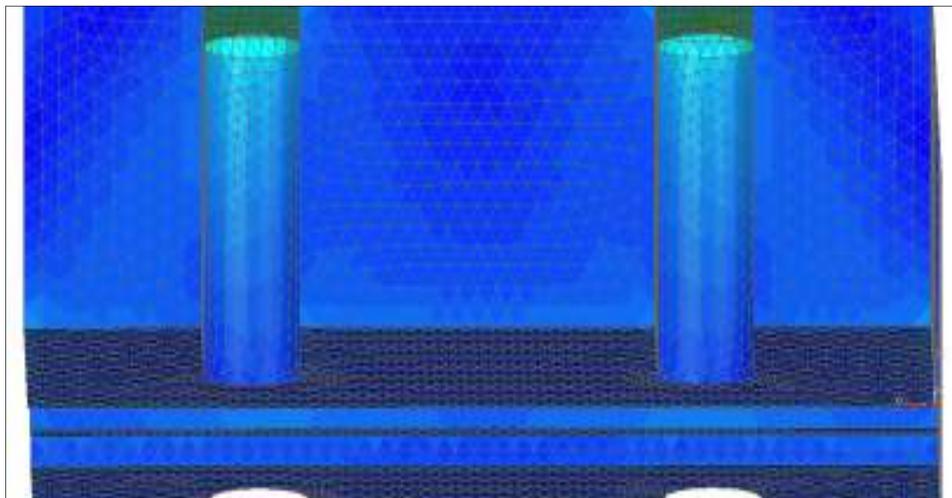
Figure 61: Von-Mises stresses in G-10 material

As stated in the prior section, the location of highest stress for the G-10 material is around the curvature of the stud cutouts. At this location the G-10 is under approximately 100-110 Mpa of stress. It is for this reason that additional loading beyond 4000 psi washer loading is not recommended. This loading limit was hypothesized after several loading iterations. One

additional factor remains that could limit the pressures applied to the test bed, the analysis of stud failure due to overloading.

Bolt Loading

Using the analysis given in Exercise 8-3 of Shigley's[8], as seen below, Equation 28 shows the force relationship between bolt stress σ_b, bolt load F_b and tensile stress area A_t.

$$\sigma_b = \frac{F_b}{A_t} \tag{28}$$

From the calculation in Appendix D, the bolt load is shown to be 67.5 kN, which when coupled with the tensile stress area from Table 8-2 of *Shigley's* for a M20 bolt, the stress within the stud is calculated to be 248.15 MPa. This is well below the selected threaded studs for the design, AISI 4140 Steel alloy M20 fully threaded studs with a minimum tensile strength of 124,000psi (855 MPa). The full stud, nut, and washer details can be found in the "Materials and Cost" section of this report. Thus at 4000 psi load the G-10 material remains the limiting design component, and ~4000 psi remains the recommended loading limit.

Finite Element Experimental Validation

For the validation of the assumptions made in FEA model, i.e. equal loading on each washers caused by nut torque and pressure monitoring throughout the G-10 including its contact with the rail, several methods are proposed. For the torquing of the nuts, it is recommended that the assembler use ultrasonic measurement techniques to measure the stud torque. This provides a direct measurement of the bolt load and not an approximation based on empirical friction data and calculations, should a torque wrench be used.   However, the ultrasonic measurement techniques could be used in conjunction with the torque wrenches in initial test bed setups to validate or disprove the effectiveness of torque wrenches for future use.

Validation of the pressure distribution upon the rail can be done a variety of ways. Two in particular are to place thin film piezoelectric pressure transducers between the rail and G-10 material at various locations along the length of the rail and compare the pressures applied to them. With repeated testing a conclusion can be drawn as to the uniformity of the rail clamping pressure and validity of the FEA models. Another method would be to use pressure indicating sensor film to directly show the variation of the pressure both on the rail or perhaps in the G-10 material blocks as well should the compressive loads be called into question.

Materials and Cost

Appendix C shows a list of suggested assembly materials, these do not include the insulation material, rail materials, or supporting beams materials. The materials are shown along with a listing of an online distributor from which they can be bought, the listed unit price, quantity needed, and total cost. The larger items mentioned have yet to be fully specified and so were not included in this cost analysis

Conclusion

After analysis of the test stand with bolt spacing of 91.6mm, 60mm washers, using steel retaining plates and G-10 insulation material, it has been shown that the assembly is able to acceptably apply even load to the rail for the purpose of validating future predictive mathematical wave propagation models. A suggested loading limit was also suggested at 4000psi per washer in order to reduce the likelihood of material deformation or failure. Suggestions were made for validating the model used, which include the use of ultrasonic bolt load monitoring and various pressure sensing techniques. The proposed test bed fulfills all design requirements given for ease of use, instrumentation placement, and size proportionality.

Appendix C: Building Materials

Component	Cost/unit	# needed	Total
Threaded Rod	$23.09	15	$346.35
Washers-58.1mm	$1.85	30	$55.50
Washers-44mm	$0.74	30	$22.2
Nuts	$0.95	60	$5.70
Steel Plates	$25.92	6	$147.74
I-Beam – Aluminum	$266.22	2	$452.44
Total			$1029.93

Table 5: Test Stand materials list

Appendix D: Sample Test Stand Calculations

Bolt load Calculations

From Equation 28,

$$F_b = P * \pi * \frac{(r_o{}^2 - r_i{}^2)}{2}$$

$$F_b = 27.58 MPa * \pi * \frac{(30^2 - 11^2)}{4 * 1000^2} = 67.497 kN$$

$$\sigma_b = \frac{67.497 kN}{272 mm^2} = 248.15 MPa$$